5-2016

Effects on a Wedge Flowmeter Installed Downstream of a Double Elbow Out of Plane

Devan S. Radle
Utah State University

EFFECTS ON A WEDGE FLOWMETER INSTALLED DOWNSTREAM OF A DOUBLE ELBOW OUT OF PLANE

by

Devan S. Radle

A thesis submitted in partial fulfillment
of the requirements for the degree

of

MASTER OF SCIENCE

in

Mechanical Engineering

Approved:

_____	_____
Dr. Robert E. Spall Major Professor	Dr. Michael C. Johnson Committee Member
_____	_____
Dr. Aaron Katz Committee Member	Dr. Mark R. McLellan Vice President for Research and Dean of the School of Graduate Studies

UTAH STATE UNIVERSITY
Logan, Utah

2016

ABSTRACT

Effects on a Wedge Flowmeter Installed Downstream of a Double Elbow Out of Plane

by

Devan S. Radle, Master of Science

Utah State University, 2016

Major Professor: Dr. Robert E. Spall
Department: Mechanical and Aerospace Engineering

Precise flow measurement is a critical part of many industries including industrial, hydropower, petroleum, nuclear, and water/wastewater. Lengthy upstream piping is required for many flowmeters to obtain accurate results. Due to piping constraints, sub-optimal flow meter installations can occur. One of these conditions is the installment of a flow meter in close proximity downstream of a double elbow out of plane (DEOP). A DEOP can cause swirl to form in the flow and can cause inaccurate metering results due to the non-uniform flow and pressure conditions. This study investigated the effect of installing a differential pressure producing wedge flow meter downstream of a DEOP on the flow measurement. Computational Fluid Dynamics (CFD) was used for this study in conjunction with physical testing.

(83 pages)

PUBLIC ABSTRACT

Effects on a Wedge Flowmeter Installed Downstream of a Double Elbow Out of Plane

Devan S. Radle

Precise flow measurement is a critical part of many industries including industrial, hydropower, petroleum, nuclear, and water/wastewater. Lengthy upstream piping is required for many flowmeters to obtain accurate results. Due to piping constraints, sub-optimal flow meter installations can occur. One of these conditions is the installment of a flow meter in close proximity downstream of a double elbow out of plane (DEOP). A DEOP can cause swirl to form in the flow and can cause inaccurate metering results due to the non-uniform flow and pressure conditions. This study investigated the effect of installing a differential pressure producing wedge flow meter downstream of a DEOP on the flow measurement. Computational Fluid Dynamics (CFD) was used for this study in conjunction with physical testing.

ACKNOWLEDGMENTS

I would like to thank all those who helped me to complete this project. Dr. Michael C. Johnson secured funding for this project and I would like to thank him for the support, encouragement, and patience in finishing this project. I would like to thank him for having the kindness of allowing a mechanical engineer a glimpse into the world of hydraulics by employing me at Utah Water Research Laboratory. My time at the UWRL has supplemented my education at Utah State University immensely with many hands on projects and learning experiences. I would also like to thank Dr. Robert Spall and Zac Sharp for the CFD pointers and help. Thanks to my wife, Kendyl, for her patience and support of me in all that I do.

Devan S. Radle

CONTENTS

LIST OF TABLES

LIST OF FIGURES

CHAPTER I

INTRODUCTION

Motivation

When determining which flowmeter technology to use, one requirement that should be considered is the upstream length of straight pipe. However, in new installments or existing installations achieving the recommended upstream length may not be possible or cost prohibitive. In existing pipelines, the available upstream distance might not be adequate for the flowmeter. To overcome the undesired flow conditions a tradeoff between cost/length and permanent pressure loss due to a flow conditioner must be analyzed, where neither is ideal. A common undesired installation condition arises from a double elbow out of plane (DEOP). A DEOP can cause swirl to form in the flow which can lead to inaccurate flow measurements. Various meter types have been researched with this adverse installation condition. One type of meter in which little research has been done is the wedge flowmeter. Figure 1 shows an illustration of a wedge flowmeter where P1 and P2 are the location of the pressure taps. P1 is the pressure tap upstream of the flow constriction and P2 is downstream. The height to diameter ratio is taken from the dimensions of *H* and *D*. This ratio is used to calculate the beta ratio, equation 1, of the meter which is the ratio of the area at the inlet of the flowmeter to the area of the flow constriction.

$$\beta = \left(\frac{1}{\pi} \left\{ \arccos\left(1 - \frac{2H}{D}\right) - 2\left(1 - \frac{2H}{D}\right)\left[\frac{H}{D} - \left(\frac{H}{D}\right)^2\right]^{\frac{1}{2}} \right\} \right)^{\frac{1}{2}} \quad (1)$$

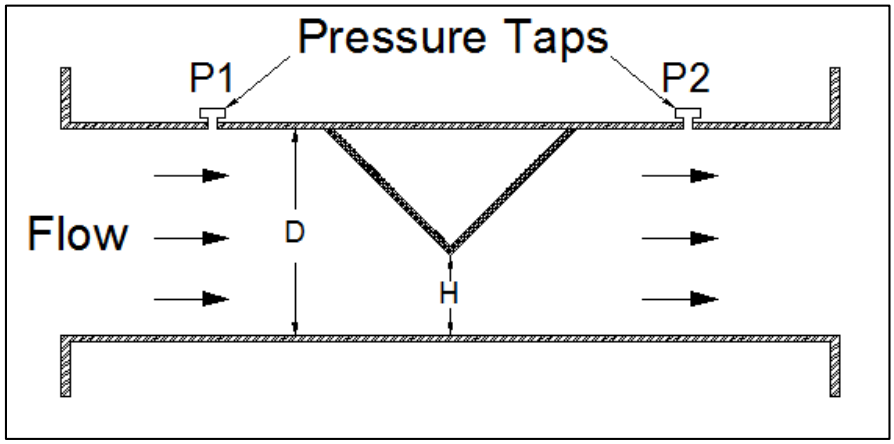

Figure 1: Wedge flowmeter illustration

The installation of this type of meter is not established in any standard. The manufacturer [1] has some installation guidelines for various types of upstream flow disturbances as shown in Table 1.

Table 1: Manufacturers installation guidelines

Flow Disturbance	Preferred		Minimum	
	Up	Down	Up	Down
1 Elbow	10	5	5	3
2 Elbows Close Coupled in-plane	10	5	5	3
3 Elbows Close Coupled out-of-plane	10	5	10	3

Wedge flowmeters are versatile meters that are designed for measuring highly viscous and abrasive fluids such as, but not limited to: sewage, sludge, cement, asphalt, tar sands, and molten sulfur. The meter is able to measure the flow of all other types of fluids, even multiphase flow. Wedge meters also are able to measure flow at a very wide range of Reynolds, measuring flows with Reynolds numbers as low as 500 [2].

Swirling flow

Swirling flow is a complex flow. Flow around a bend creates an asymmetrical velocity profile. The flow going around a bend is forced against the outside wall of the bend and then produces vortices. A DEOP causes a single vortex to form. This is known as swirling flow. This is shown in Figure 2. Two close coupled elbows in perpendicular planes is a disturbance that causes swirling flow to occur. The decay of the swirl has been extensively studied and modeled. According to Michael Reader-Harris [3] "a computational model has been developed that correlates well with experimental data. According to the computational model, an 18° swirl (a typical value immediately downstream of a double elbow out of plane) will decay to 2° after 200 diameters." According to ISO 5167 [4], a swirl free flow exists when the swirl angle at all points over the pipe cross-section is less than 2°.

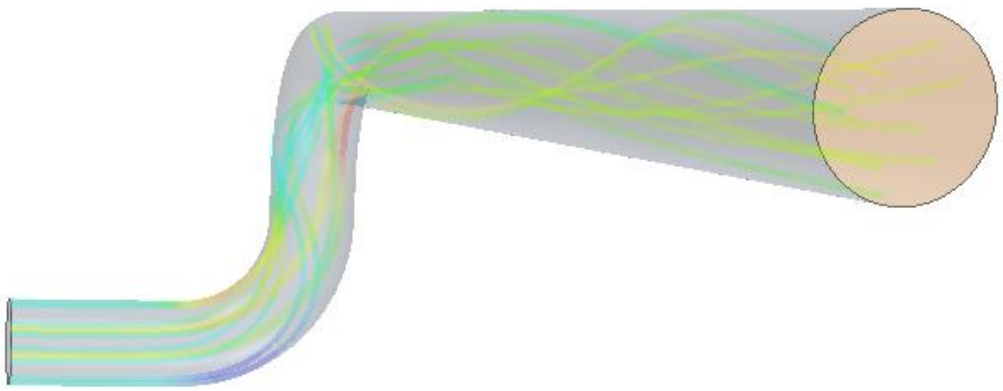

Figure 2: Streamlines 11 *ft/s* DEOP

Bernoulli's Principle

Differential pressure producing flow meters relate Bernoulli's equation, conservation of mass to the differential pressure to measure flow. The flowmeter consists of some type of constriction that causes the velocity of the flow to increase. Bernoulli's principle illustrates that as the velocity of the fluid increases the pressure must decrease. Equation 2 is Bernoulli's equation assuming incompressible horizontal flow and neglecting the any difference in height between the two points of measurement.

$$P_1 + \frac{1}{2}\rho V_1^2 = P_2 + \frac{1}{2}\rho V_2^2 \quad (2)$$

Here, P is pressure, $V$is velocity of the flow, and ρ is the density of the fluid. The conservation of mass for an incompressible fluid is shown in Equation 3.

$$Q = V_1 A_1 = V_2 A_2 \quad (3)$$

Here, Q is the volumetric flowrate and A is the flow area. After combining Equations 2 and 3 the ideal flowrate is obtained (Equation 4).

$$Q_{ideal} = A_2 \sqrt{\frac{2(P_1 - P_2)}{\rho(1 - \beta^4)}} \quad (4)$$

Here β is the beta ratio of the flowmeter as described by Equation 1, H is the height of the flow area in the constriction of the flowmeter and D is the diameter of the flowmeter upstream of the constriction as illustrated in Figure 1.

If no losses are taken into account, erroneous results will be obtained by over predicting the flow rate. Due to pressure losses from frictional effects as well as the vena contracta area being smaller than the flow area of the constriction, a correction factor must be used. This correction factor, known as the discharge coefficient *C* takes up the losses as illustrated in Equation 5.

$$C = \frac{Q_{actual}}{Q_{ideal}} \tag{5}$$

Substituting Equation 4 into Equation 5 results in Equation 6.

$$C = \frac{Q_{actual}}{\frac{A\sqrt{2g\Delta h}}{\sqrt{1-\beta^4}}} \tag{6}$$

In Equation 6, the differential pressure is converted in to Δh, the head differential, and g is the gravitational acceleration constant.

Yoon et al. [5] conducted a study investigating the discharge coefficient of five different wedge flow meters. By doing so a relationship was found between discharge coefficient and different height to diameter ratios (*H*/*D*). This relationship is expressed in Equation 7 where *H/D* ranges from 0.3 to 0.7.

$$C = 0.91136\left(\frac{H}{D}\right)^{0.1303} - 23.363\left(\frac{H}{D}\right)^{4} + 50.378\left(\frac{H}{D}\right)^{3} - 37.246\left(\frac{H}{D}\right)^{2} + 11.062\left(\frac{H}{D}\right) - 1.105 \tag{7}$$

Research Overview

To establish a baseline for comparison, a straight pipe calibration was used. This data was used to compare the physical results as well as the CFD results. Different beta ratios were simulated.

List of Tasks

1. Conduct literature review
2. Laboratory test a 12 inch wedge flowmeter at zero and five diameters downstream of a DEOP.
3. Test meter with pressure taps in different positions.
4. Establish appropriate baseline performance for comparison.
5. Run CFD simulations with differing turbulence models for validation.
6. Run simulations on flow meters with a 0.5 and 0.6 beta ratio

CHAPTER II

LITERATURE REVIEW

As part of this research, a literature review was carried out to discover what research has already been established with respect to this topic. Through the resources provided by the USU library and online databases, information has been discovered to support this research. ISO 5167 and ASME MFC-3M are both standards that specify the installation conditions of orifice plates, Venturi tubes and nozzles. Also some literature has been found to support the use of CFD to model the effects of installation. A CFD study done by Hilgestock and Ernst[6] showed that "When using advanced turbulence models the numerical data agree very well with experimental findings at least for the double bend out-of-plane."

There is some literature in which the V-cone and orifice flowmeters were the subjects of research downstream of a DEOP. Gibson and Reader-Harris [7] conducted a study on Venturi tubes of convergent angle of 10.5° and 21° comparing CFD to experimental data of change in *C*, the discharge coefficient. However, other internal geometries of commercially available Venturi tubes such as the classical Venturi, HVT-Halmi Venturi, and the Universal Venturi Tube could be investigated in a similar manner.

Banchhor et al. [8] used CFD to investigate the performance characteristics of wedge flow meters with varying geometries. They used the standard k-ε model available in the general purpose solver Fluent. The effects of wedge vertex angle, vertex radius, H/D ratio, and inlet velocity profile were simulated. Only the geometry of a 60° wedge element with a 3 mm vertex radius and an *H/D* ratio of 0.5 was used to investigate the

effect of swirl. To create the swirl, the tangential velocity of the flow was varied from 5% to 20% of the axial velocity of the flow. The results of Banchhor et al. state “The discharge coefficient with 5% swirl was found as 0.806. With increase in swirl to 10%, 15% and 20%, discharge coefficient has changed to 0.802, 0.801 and 0.801 respectively.”

After an extensive review, various studies on installation effects were found for different meter types. However, there are limited studies available on a wedge flowmeter with a sharp 90° wedge element installed downstream of a DEOP.

CHAPTER III

EXPERIMENTAL SETUP

Physical Test Setup

The physical tests of this study were performed at the Utah Water Research Laboratory (UWRL). The physical flowmeter used was a 12 inch 0.60 beta ratio Primary Flow Signal (PFS) wedge meter. The objectives of the experiment were to determine the value of the discharge coefficient of a wedge flowmeter located zero and five diameters downstream of a DEOP. Figure 3 is a picture taken of the test set up. A reference 12-inch magnetic flowmeter was used with 20 diameters of pipe both upstream and downstream to ensure a fully developed profile entering the DEOP. Due to the available elbows at hand, the first elbow had a five inch extension on the downstream end.

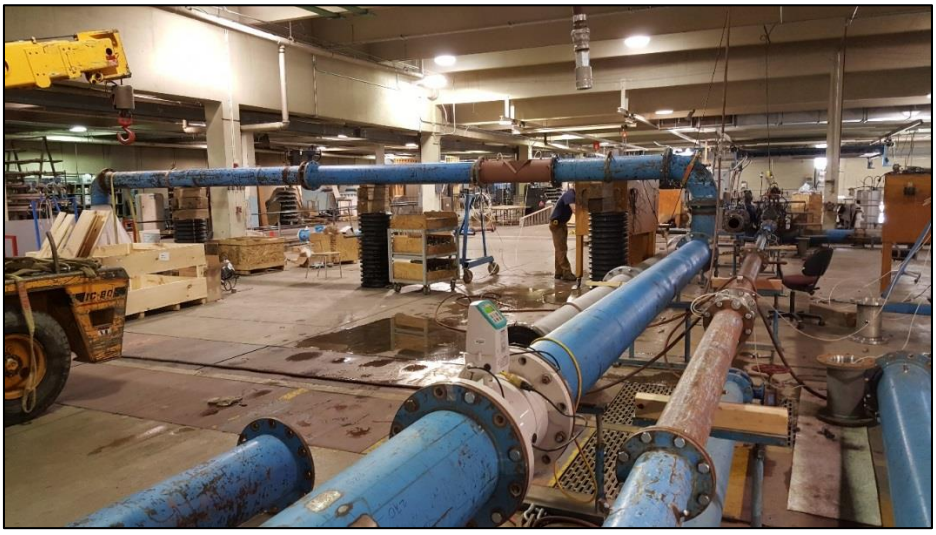

Figure 3: Laboratory Flowmeter Installation

The flowmeter was tested in four different configurations. Primarily, the flowmeter was in the vertical position with the two pressure taps in the same plane as the second elbow as shown in Figure 4 and Figure 5. The secondary position that was tested was with the flow meter rotated 90° clockwise as shown in Figure 6 (pressure taps out of plane). In both positions the meter was tested at five and zero diameters downstream of the DEOP.

Figure 4: Wedge Flowmeter Close Coupled to DEOP in the Vertical Position

Figure 5: Wedge Flowmeter Five Diameters Downstream to DEOP in the Vertical Position

Figure 6: Horizontal or Out-of-Plane Installation of Wedge Flowmeter

Test Procedure

The Coefficient for the flowmeter was then found over a range of different flows. This was done by varying the flowrate through the meter by use of a downstream control valve. The flow ranged, in terms of pipe Reynolds numbers, from 66,000 up to 1,300,000. The flow rate was determined by the calibrated magnetic flowmeter placed 20 diameters upstream of the DEOP. The differential pressure across the flow meter was measured using a Rosemount pressure transmitter.

CHAPTER IV

COMPUTATIONAL FLUID DYNAMICS

The general purpose CFD program, STAR-CCM+, was used in this study [9]. There are various turbulence models available in STAR-CCM+. An appropriate choice of turbulence model that produces accurate results with an acceptable computational cost is a question that also must be considered in industry today. For this reason, differing turbulence models were selected and used. The following turbulence models were used: Realizable k-ε, Reynolds Stress, and k-ε: Elliptic Blending Model.

Geometry

The intrinsic 3D-CAD package in STAR-CCM+ as well as AutoCAD were used to create the geometries used in the simulations. At the inlet of each geometry used, two diameters of straight pipe were used before any bends or, for the straight pipe simulations, flowmeters. The outlet for each simulation was located six diameters downstream of the end of the flowmeter. Dimensions for the geometry of the flowmeter were taken from the Primary Flow Signal drawing for the meter. The locations of the pressure taps and wedge angle were held constant for the different beta ratio meters that were tested, only the *H/D* ratio was changed. The geometry of the DEOP used in the simulations was made to reflect the physical pipe line. No scaling of the geometry was used.

Meshing

All meshing was done by STAR-CCM+. To make a fair comparison between the various turbulence models, the meshes for the different simulations had the same basic setup. The polyhedral and prism layer mesh were used for all simulations.

The polyhedral meshing model is created from an underlying tetrahedral mesh. The average polyhedral cell has 14 faces and a polyhedral mesh has roughly five times less cells than a tetrahedral mesh for a given surface.

The prism layer mesh model is used to make orthogonal prismatic cells on the wall surfaces of the simulation. These cells aid in resolving the near wall flow of the viscous sublayer were velocity gradients are steep. The prism layer directly influences the wall y+ parameter, which is a non-dimensional parameter used to relate flow velocity and cell size. The pressure near the wall were of interest for this study, therefore the wall y+ values were less than or equal to one. This was accomplished by refining the prism layer until the appropriate wall y+ value was met.

The surface remesher was used for many of the simulations. This model improves the overall quality of a surface and optimizes it for the volume mesh. Surface refinement was achieved by increasing the basic curvature reference value. The basic curvature value defines the face size on a curve as the circumference of and equivalent circle divided by the user defined number of Pts/circle. This model aided in limiting the cell size around the walls of the simulation, especially in the area of the volumetric control.

Some volumetric grid refinement was employed to refine the area of the flowmeter. This was done due to the high velocity and pressure gradients that are to be found in this region due to the constriction of the wedge.

Mesh Reference Values

The Grid Convergence Index method was used for the grid refinement analysis of this study. Therefore, three successively finer meshes were used for each test condition. Tables 2, 3, and 4 show the reference values used for the various simulations. All reference values associated with the prism layer were held constant for all meshes. These values can be found in Table 5.

Table 2: Straight Pipe Simulation Mesh Reference Values

0.6 Beta - Straight			
Reference Value	Mesh 3	Mesh 2	Mesh 1
Base Size	1.0 in	0.5 in	.26 in
Volumetric Control	50%	50%	50%
0.5 Beta - Straight			
Reference Value	Mesh 3	Mesh 2	Mesh 1
Base Size	1.0 in	0.6 in	.35 in
Volumetric Control	50%	50%	50%
Surface Curvature	50 pts/circle	50 pts/circle	50 pts/circle
0.7 Beta - Straight			
Reference Value	Mesh 3	Mesh 2	Mesh 1
Base Size	1.0 in	0.6 in	.35 in
Volumetric Control	50%	50%	50%
Surface Curvature	50 pts/circle	50 pts/circle	50 pts/circle

Table 3: Close Coupled Simulations Mesh Reference Values

0.6 Beta - Close Coupled			
Reference Value	Mesh 3	Mesh 2	Mesh 1
Base Size	2 in	1 in	.345 in
Volumetric Control	25%	50%	50%
Surface Curvature	100 pts/circle	100 pts/circle	100 pts/circle
0.5 Beta - Close Coupled			
Reference Value	Mesh 3	Mesh 2	Mesh 1
Base Size	1 in	.5 in	0.35
Volumetric Control	50%	50%	50%
Surface Curvature	60 pts/circle	60 pts/circle	60 pts/circle
0.7 Beta - Close Coupled			
Reference Value	Mesh 3	Mesh 2	Mesh 1
Base Size	2 in	.5 in	0.35
Volumetric Control	25%	50%	50%
Surface Curvature	100 pts/circle	100 pts/circle	100 pts/circle

Table 4: Five Diameters Simulations Mesh Reference Values

0.6 Beta - 5 Diameters			
Reference Value	Mesh 3	Mesh 2	Mesh 1
Base Size	2 in	1 in	.343 in
Volumetric Control	25%	50%	49%
Surface Curvature	100 pts/circle	100 pts/circle	100 pts/circle
0.5 Beta - 5 Diameters			
Reference Value	Mesh 3	Mesh 2	Mesh 1
Base Size	1 in	0.5 in	.34 in
Volumetric Control	50%	50%	50%
Surface Curvature	60 pts/circle	60 pts/circle	60 pts/circle
0.7 Beta - 5 Diameters			
Reference Value	Mesh 3	Mesh 2	Mesh 1
Base Size	1 in	0.5 in	.34 in
Volumetric Control	50%	50%	49%
Surface Curvature	60 pts/circle	60 pts/circle	60 pts/circle

Table 5: Prism Layer Reference Values

Option	Value
Prism Layers	20
Prism layer Stretching	1.5
Prism Layer Thickness	0.125 ft

Physics

The primary equations used in solving the motion of fluids are the Reynolds-Averaged Navier-Stokes equations. These are the primary equations that are used in by Star CCM+ to solve the flow field. In the simulations created for this research, only the incompressible Newtonian fluid water was used. A second-order upwinding scheme was used for the transport equations and convection terms. The coupling of the pressure and velocity was completed with the SIMPLE algorithm. The fluid properties used were those associated with water at 45 degrees Fahrenheit which is near the water temperature used for the physical tests. The density of the water used in the simulations was set equal to 62.42 *lb/ft*^3 and the dynamic viscosity was set equal to 1.4184 *cP*.

Turbulence Models

One of the turbulence models that was used was the Realizable k-ε model. This is a two equation model that was developed by Shih at NASA Lewis [10] and is implemented by varying $C\mu$, a constant in the eddy viscosity equation, spatially. This model is more accurate and performs better for swirling and rotating flows, and separated flows than the standard k-ε model.

The Reynold Stress Transport model is the most complex and complete Reynolds-averaged Navier-Stokes turbulence model. This is a seven equation model that is able to

capture swirling flows and other anisotropy [9]. However, this model is computationally expensive and is more difficult to converge.

The k-ε: Elliptic Blending Model is a four equation model extension of the k-ε model that is an accurate predictor of near wall turbulence and separation. This model is similar to the V2F model, but differs in wall treatment. The V2F variant of the k-ε model is a model that more accurately predicts the effects of near wall turbulence which is crucial for the accurate prediction of heat transfer, skin friction and flow separation [9]. The Elliptic Blending Model handles non-local wall effects with an elliptic blending approach rather than the elliptic relaxing V2F approach. The Elliptic Blending Model is also more robust than the V2F model.

Even though the wall y+ values for all simulations were less than or equal to one, the all y+ wall treatment version of each turbulence model was used. The k-ε based turbulence models are based on Boussinesq's isotropic eddy viscosity assumption. Therefore, it can be expected that these turbulence models will have difficulty with swirling flows.

Fully Developed Simulations

To save on computational time and resources fully developed flow profiles were created for the different flow velocities. A periodic interface was used where the mass flow rate was defined to correlate the appropriate flow through the simulations. These simulations were run until a fully developed profile was achieved. This fully developed profile was then used as the input to the various simulations. Figure 7 shows a fully

developed flow profile used in this study with an average flow velocity of 11 *ft/s* in a 12 inch diameter pipe.

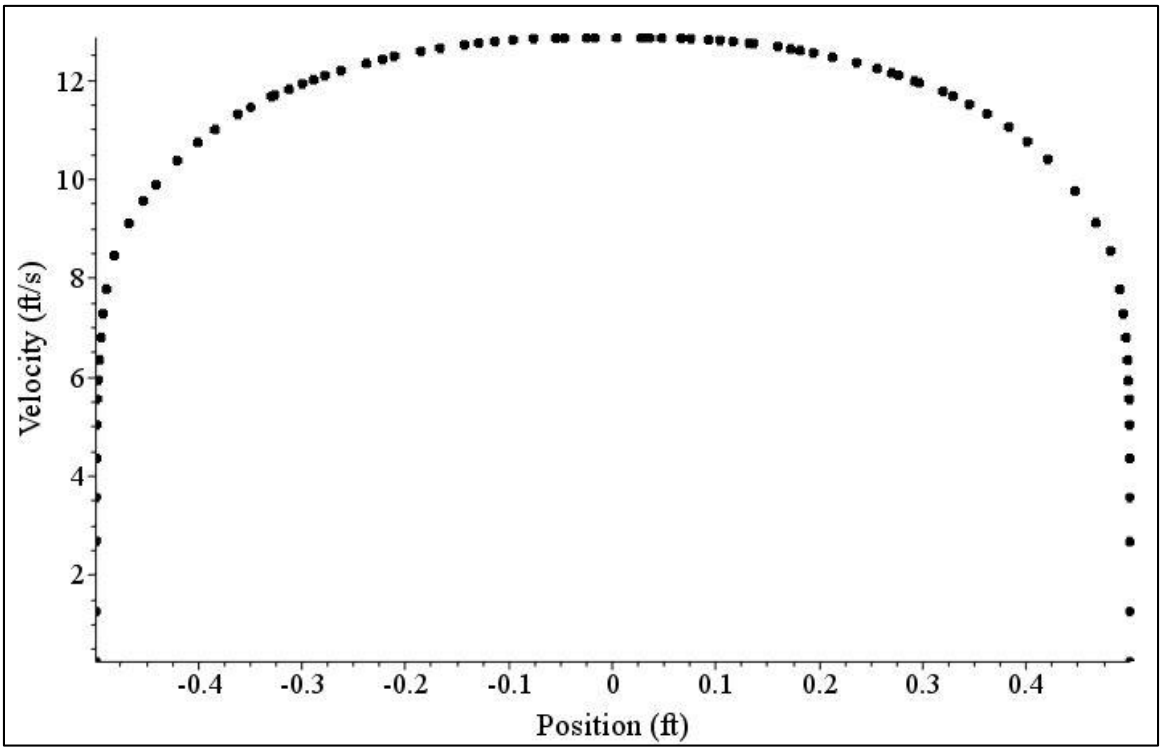

Figure 7: Velocity profile for a 12 inch diameter pipe using the k-ε model at a Reynolds number of 720,000

CFD Calculations

Rather than conducting all of the calculations to find the coefficient in Star-CCM+, certain values were taken from the simulation and imported into a spreadsheet. The values that were extracted from the simulation were the mass flow rate, the differential pressure, the upstream area and the throat area. The areas were taken for each

simulation as these values are dependent upon the mesh of the simulation. The areas are necessary for the calculation of the beta ratio.

Grid Convergence Index

The Grid Convergence Method is a method of determining the uncertainty of a simulation due to the refinement of the grid. It is the method of choice for the Journal of Fluid Engineering and is a generally accepted method. For a more in depth explanation of the following see [11]. The results were calculated in Matlab. The function used to do the calculations is found in Appendix D. The procedure is as follows:

Step 1: Define a representative cell, mesh or grid size *h*.

Step 2: Select three significantly different grid sizes. It is recommended that the refinement factor $r = h_{coarse}/h_{fine}$ is greater than or equal to 1.3. This value is not formally derived but is based upon experience.

Step 3: Calculate the apparent order, *p*, of the method.

Step 4: Calculate the extrapolated values.

Step 5: Calculate and report the error estimates.

The results of this method are included in the Results chapter.

Iterative Convergence

Iterative convergence is considered to be achieved when the normalized residuals for each equation being solved decreases by at least three orders of magnitude. This criteria was met for all simulations as well as that all values used for calculating *C* remained constant in the 6^{th} significant digit.

CHAPTER VI

RESULTS

The CFD results given are the extrapolated values from the GCI method. Simulations were run at three different flow velocities. For the comparison of the three turbulence models, the 0.6 beta ratio flow meter was used. This was done to determine which turbulence model best represented the physical data. The k-ε turbulence model was selected as the turbulence model that best represented the physical data. Therefore, for the 0.5 and 0.7 beta ratio meters only the k-ε turbulence model was used.

Laboratory Results

Figure 8 shows the physical data taken in the laboratory. The effects of installing the flowmeter in different locations and positions downstream of the DEOP are shown. Negligible effects are observed, as compared to the straight pipe calibration, when the flowmeter is installed five diameters downstream of the DEOP. At five diameters downstream the percent change in the coefficient for the flowmeter was 0.19% when the pressure taps were in plane with the second elbow and 0.02% when the pressure taps were out of plane with the second elbow. At five diameters downstream, the orientations of the installation are also negligible as similar results are achieved when comparing the results of the in-plane data with the out-of-plane data. However, the orientation of the flowmeter does have an effect when the flowmeter is close coupled to the DEOP. By rotating the flowmeter 90 degrees into the horizontal or out-of-plane position, the effect of the DEOP is reduced. The percent change in coefficient for the flowmeter when it is close coupled to the DEOP when the pressure taps are in plane with the second elbow is

1.38%. When the pressure taps are out of plane with the second elbow in the DEOP the percent change in coefficient is 0.36%. The only significant trend in the coefficient with Reynolds number occurred with the close coupled in-plane data set. All other data sets show no significant trend with Reynolds number.

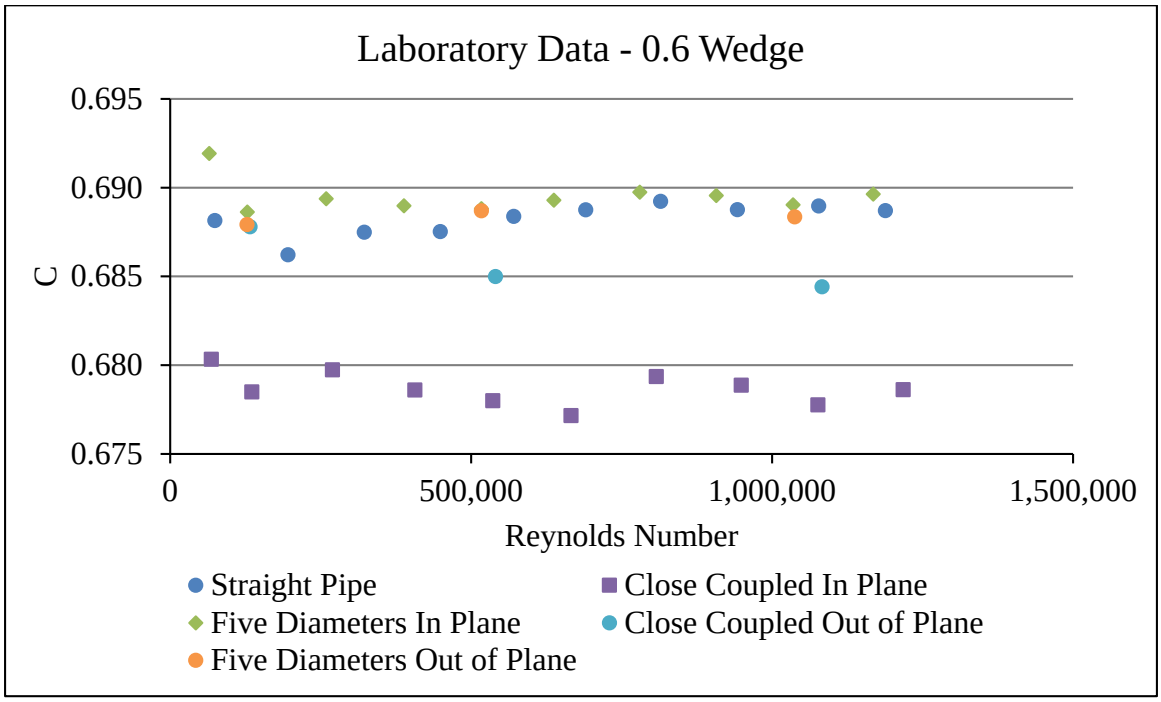

Figure 8: Laboratory Data

The tabulated laboratory results are found in Table 6 - 8. The uncertainty for each data point is included in these tables. The uncertainty for the laboratory data was calculated following ASME 19.1-2005.

Table 6: Straight Pipe Laboratory Results and Uncertainty

Straight Pipe		
Inlet Reynolds Number	C	Uncertainty %
74,634	0.6881	0.18%
196,036	0.6862	0.19%
322,830	0.6875	0.12%
448,973	0.6875	0.13%
570,960	0.6884	0.11%
690,738	0.6887	0.14%
815,063	0.6892	0.12%
942,766	0.6887	0.11%
1,077,614	0.6890	0.11%
1,188,688	0.6887	0.10%

Table 7: In-Plane Laboratory Results and Uncertainty

Close Coupled, In-Plane			Five Diameters, In Plane		
Inlet Reynolds Number	C	Uncertainty %	Inlet Reynolds Number	C	Uncertainty %
68,711	0.6803	0.29%	64,887	0.6919	0.30%
135,937	0.6785	0.26%	128,319	0.6886	0.26%
269,799	0.6797	0.29%	259,272	0.6894	0.29%
406,870	0.6786	0.27%	388,586	0.6890	0.27%
536,372	0.6780	0.26%	517,043	0.6888	0.26%
666,353	0.6771	0.26%	637,538	0.6893	0.26%
807,991	0.6794	0.27%	780,234	0.6897	0.27%
949,150	0.6789	0.27%	907,466	0.6896	0.27%
1,076,417	0.6778	0.26%	1,035,005	0.6890	0.26%
1,218,215	0.6786	0.26%	1,168,055	0.6896	0.26%

Table 8: Out-of-Plane Laboratory Results and Uncertainty

Close Coupled, Out-of-Plane			Five Diameters, Out-of-Plane		
Inlet Reynolds Number	C	Uncertainty %	Inlet Reynolds Number	C	Uncertainty %
132,887	0.6878	0.63%	127,921	0.6879	0.26%
540,683	0.6850	0.26%	517,349	0.6887	0.26%
1,083,443	0.6844	0.26%	1,037,761	0.6883	0.26%

Straight Pipe Simulations

Figure 9 displays and compares the results of the CFD simulations versus the physical data obtained in the lab. For these simulations the same meshes were used for the different turbulence models. The Elliptic Blending model at first appears to show a trend with Reynolds number, however upon examining the GCI calculations in Table 9 the trend is not valid. The uncertainty due to the mesh refinement for the 720k and 332k simulations are 3.09% and 2.33% respectively. The general shift upwards of the CFD results as compared to the physical data occurs for all simulations in this study.

Table 9: Summary of GCI calculations for C for Straight Pipe Simulations

Straight Pipe Simulations - GCI										
Simulation	r_{21}	r_{32}	C_3	C_2	C	C_{ext}^{21}	p	e_a^{21}	e_{ext}^{21}	GCI_{fine}^{21}
48k K-Epslion	1.31	1.31	0.702	0.703	0.702	0.701	4.104	0.16%	0.08%	0.10%
48k Elliptic Blending	1.31	1.31	0.702	0.697	0.701	0.714	0.989	0.57%	1.83%	2.33%
48k Reynolds Sress	1.31	1.31	0.705	0.704	0.704	0.704	5.123	0.03%	0.01%	0.01%
332k K-Epsilon	1.31	1.31	0.701	0.702	0.701	0.697	1.019	0.19%	0.61%	0.76%
332k Elliptic Blending	1.31	1.31	0.702	0.703	0.701	0.695	1.374	0.35%	0.79%	0.98%
332k Reynolds Stress	1.31	1.31	0.704	0.703	0.704	0.704	1.599	0.05%	0.09%	0.12%
720k K-Epsilon	1.31	1.31	0.702	0.702	0.702	0.702	7.861	0.01%	0.00%	0.00%
720k Elliptic Blending	1.31	1.31	0.701	0.703	0.701	0.684	0.403	0.28%	2.53%	3.09%
720k Reynolds Stress	1.31	1.31	0.702	0.703	0.704	0.704	1.550	0.06%	0.12%	0.16%

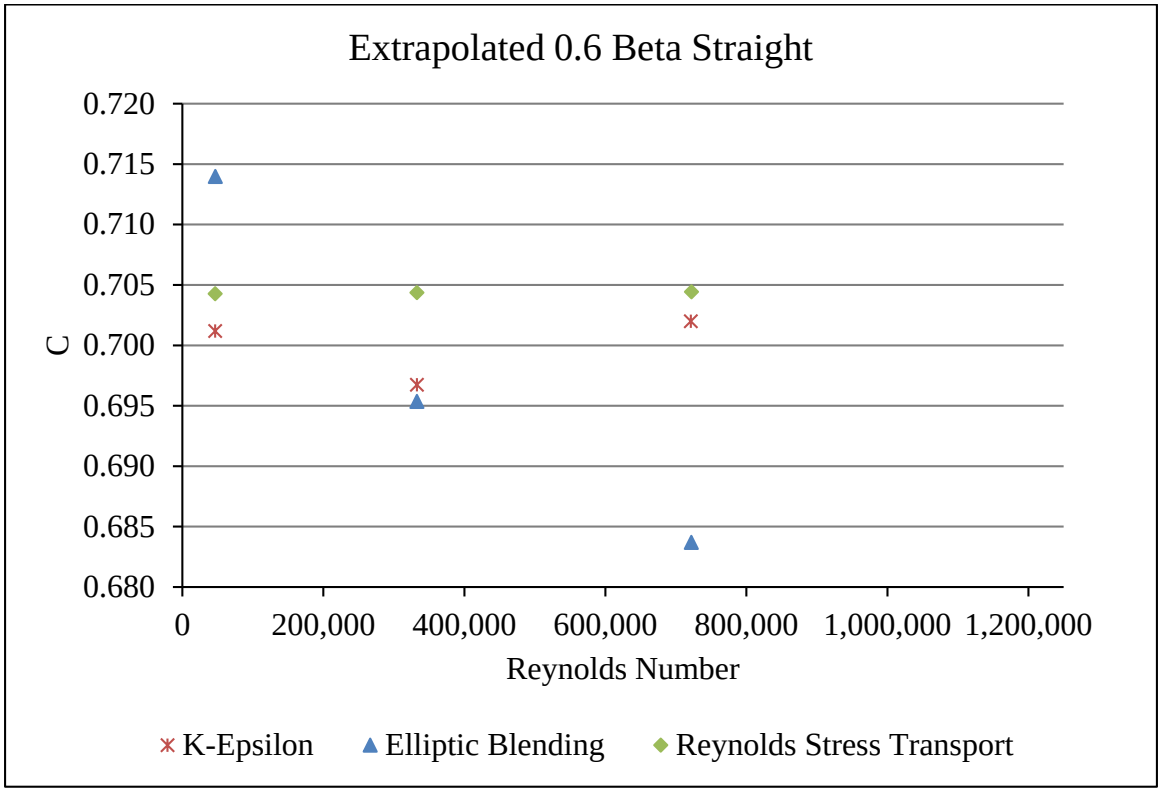

Figure 9: Straight Pipe CFD Results for 0.6 Beta Flowmeter

Table 10: Statistical Analysis for Straight Pipe GCI calculations

Overall Statistical Analysis - Straight				
	p	e_a^{21}	e_{ext}^{21}	GCI_{fine}^{21}
Average	2.669	0.19%	0.67%	0.84%
Standard Deviation	2.352	0.18%	0.86%	1.07%
Minimum	0.403	0.01%	0.00%	0.00%
Maximum	7.861	0.57%	2.53%	3.09%

Close Coupled Simulations

A similar trend can be seen in the results of close coupled simulations in Figure 10. The CFD results are about 2% higher than the physical data. However the uncertainty

due to the mesh refinement as shown in Table 11 is lower. The highest uncertainty occurs with the Elliptic Blending model. It is also noteworthy that the Reynold Stress Transport simulations had the lowest uncertainty, but were the farthest away from the physical data. The average uncertainty for these simulations was 0.25% with a maximum of 1.00% as shown in Table 12.

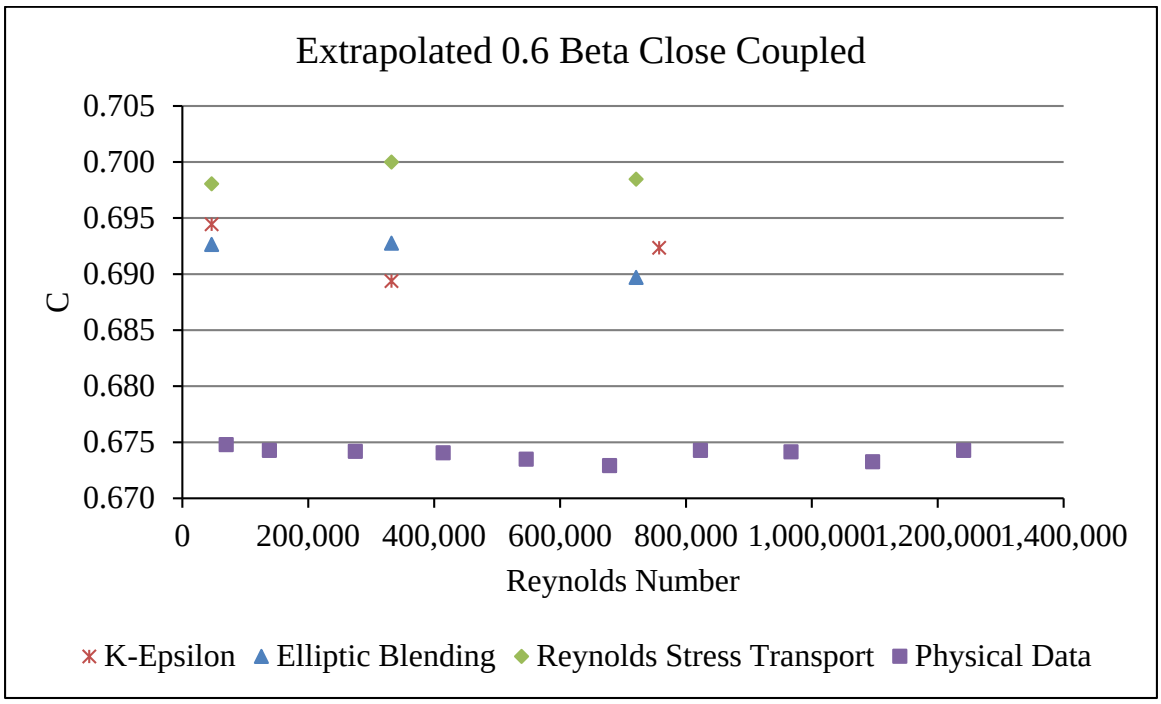

Figure 10: Close Coupled CFD Results 0.6 Beta Ratio Flowmeter

Table 11: Summary of GCI calculations for C for Close Coupled Simulations

Close Coupled Simulations - GCI										
Simulation	r_{21}	r_{32}	C_3	C_2	C_1	C_{ext}^{21}	p	e_a^{21}	e_{ext}^{21}	GCI_{fine}^{21}
48k K-Epslion	1.31	1.31	0.692	0.691	0.693	0.694	3.459	0.30%	0.20%	0.25%
48k Elliptic Blending	1.31	1.31	0.698	0.700	0.698	0.693	1.081	0.27%	0.81%	1.00%
48k Reynolds Sress	1.31	1.31	0.705	0.698	0.698	0.698	10.682	0.06%	0.00%	0.00%
332k K-Epsilon	1.31	1.31	0.692	0.690	0.690	0.689	3.050	0.08%	0.06%	0.08%
332k Elliptic Blending	1.31	1.31	0.693	0.693	0.693	0.693	5.677	0.04%	0.01%	0.01%
332k Reynolds Stress	1.31	1.31	0.699	0.699	0.699	0.700	3.004	0.12%	0.09%	0.12%
720k K-Epsilon	1.31	1.31	0.693	0.691	0.692	0.695	1.352	0.16%	0.37%	0.46%
720k Elliptic Blending	1.31	1.31	0.693	0.692	0.692	0.690	1.374	0.12%	0.26%	0.32%
720k Reynolds Stress	1.31	1.31	0.699	0.698	0.698	0.698	4.472	0.02%	0.01%	0.01%

Table 12: Statistical Analysis for Close Coupled GCI calculations

Overall Statistical Analysis - Close Coupled				
	p	e_a^{21}	e_{ext}^{21}	GCI_{fine}^{21}
Average	3.795	0.13%	0.20%	0.25%
Standard Deviation	2.827	0.09%	0.25%	0.30%
Minimum	1.081	0.02%	0.00%	0.00%
Maximum	10.682	0.30%	0.81%	1.00%

Five Diameters Downstream Simulations

Figure 11 shows the CFD results of the 0.6 beta ratio flowmeter located five diameters downstream of the DEOP for the various turbulence models. The k-ε turbulence model had values that most closely approached the physical data. The values for the k-ε and Elliptic Blending models at 332,000 Reynolds number are the outliers in this data set, they have an uncertainty of 2.99% and 3.00% respectively. The results at 48,000 Reynolds number had a very low uncertainty as shown in Table 13. Table 14 shows the overall statistical analysis of this set of data.

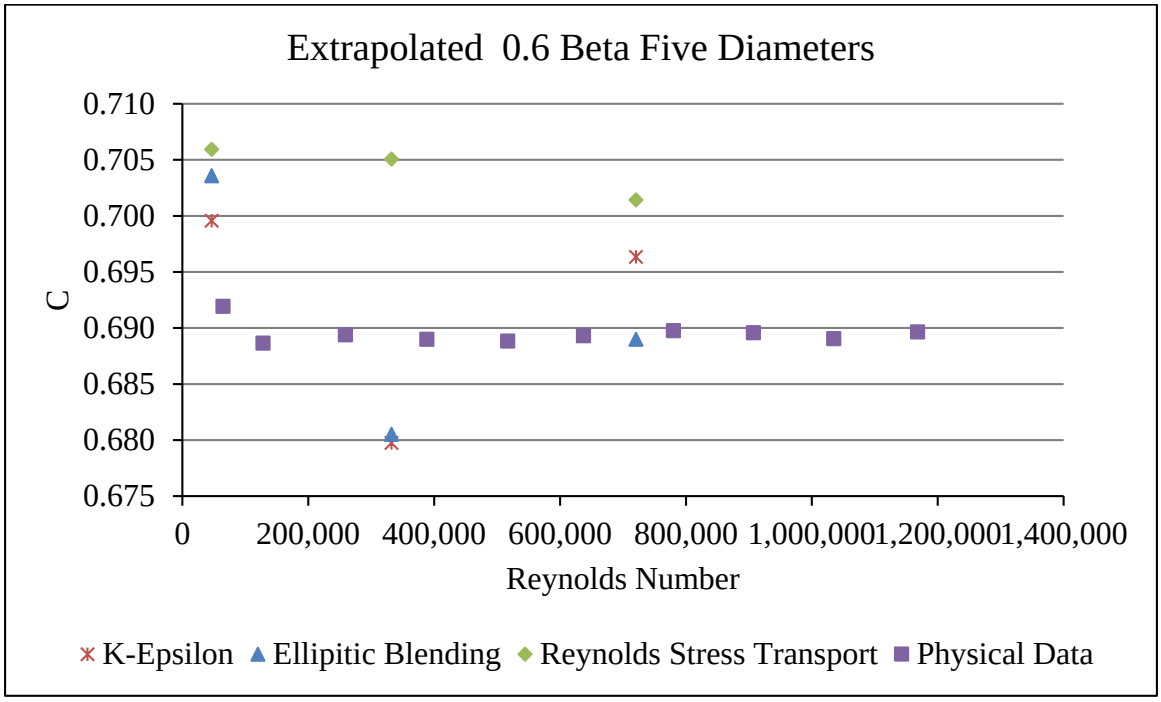

Figure 11: Close Coupled CFD Results 0.6 Beta Ratio Flowmeter

Table 13: Summary of GCI calculations for C for Five Diameter Simulations

Five Diameters Downstream - GCI										
Simulation	r_{21}	r_{32}	C_3	C_2	C_1	C_{ext}^{21}	p	e_a^{21}	e_{ext}^{21}	GCI_{fine}^{21}
48k K-Epslion	1.30	1.30	0.703	0.700	0.700	0.700	6.441	0.08%	0.02%	0.02%
48k Elliptic Blending	1.30	1.30	0.708	0.704	0.704	0.704	11.899	0.03%	0.00%	0.00%
48k Reynolds Sress	1.30	1.30	0.709	0.706	0.706	0.706	10.652	0.03%	0.00%	0.00%
332k K-Epsilon	1.30	1.30	0.702	0.700	0.696	0.680	0.680	0.47%	2.45%	2.99%
332k Elliptic Blending	1.30	1.30	0.704	0.701	0.697	0.681	0.743	0.52%	2.46%	3.00%
332k Reynolds Stress	1.30	1.30	0.708	0.705	0.705	0.705	18.026	0.00%	0.00%	0.00%
720k K-Epsilon	1.30	1.30	0.703	0.700	0.696	0.688	1.610	0.59%	1.14%	1.41%
720k Elliptic Blending	1.30	1.30	0.703	0.701	0.694	0.689	3.009	0.92%	0.76%	0.95%
720k Reynolds Stress	1.30	1.44	0.708	0.705	0.703	0.701	2.703	0.29%	0.17%	0.22%

Table 14: Statistical Analysis for Five Diameter GCI calculations

Overall Statistical Analysis - Five Diameters				
	p	e_a^{21}	e_{ext}^{21}	GCI_{fine}^{21}
Average	6.196	0.33%	0.78%	0.95%
Standard Deviation	5.734	0.30%	0.97%	1.19%
Minimum	0.680	0.00%	0.00%	0.00%
Maximum	18.026	0.92%	2.46%	3.00%

0.5 Beta Ratio

Figure 12 shows the CFD results for the 0.5 Beta ratio flowmeter. This geometry was simulated only and was not physically tested in the lab. Table 16 shows the uncertainty of the simulations. The average uncertainty in Table 15 is a very small 0.05%. The k-ε turbulence model closely matched the physical data for the 0.6 beta ratio data, therefore, the 0.5 beta ratio simulations were modeled only with the k-ε turbulence model. The same trend of a lower coefficient for the closed coupled simulations is followed with this flowmeter. Also the five diameter simulations show less of an effect on the flowmeter.

Table 15: Statistical Analysis for 0.5 Beta Ratio Simulations

Overall Statistical Analysis - 0.5 Beta Ratio				
	p	e_a^{21}	e_{ext}^{21}	GCI_{fine}^{21}
Average	7.925	0.09%	0.04%	0.05%
Standard Deviation	4.934	0.11%	0.05%	0.07%
Minimum	1.194	0.00%	0.00%	0.00%
Maximum	20.080	0.32%	0.14%	0.17%

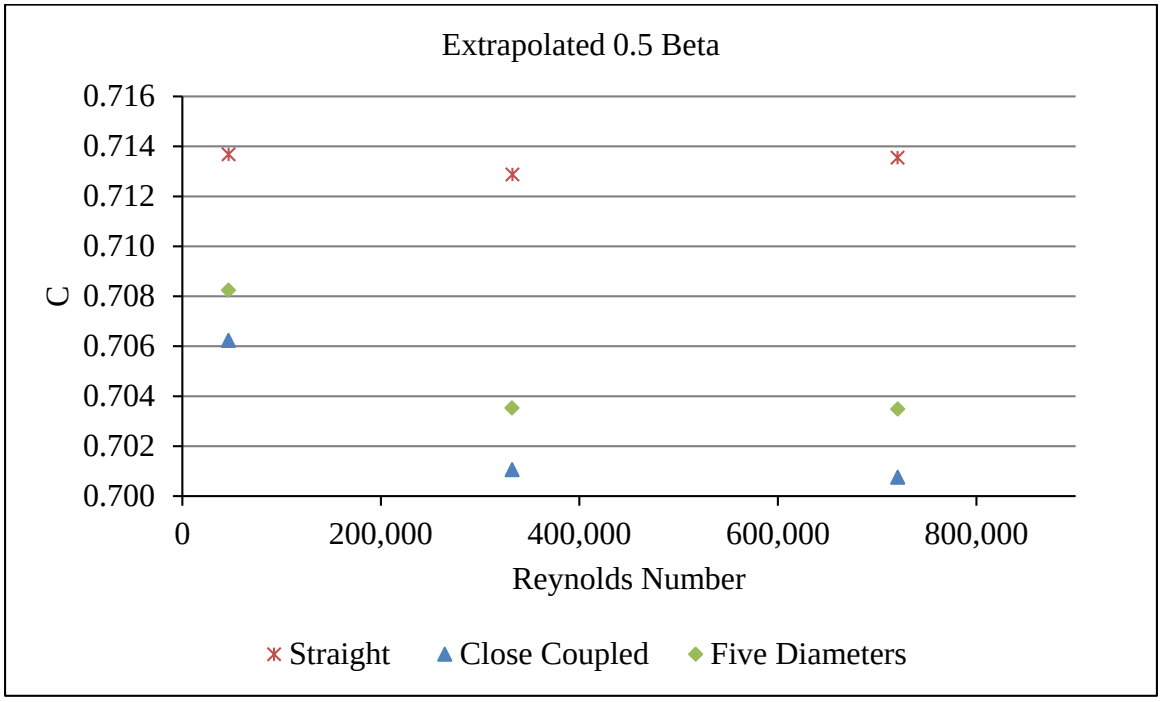

Figure 12: CFD Results 0.5 Beta Ratio Flowmeter

Table 16: Summary of GCI calculations for C for 0.5 Beta Ratio Simulations

0.5 Beta Ratio Simulations - GCI										
Simulation	r_{21}	r_{32}	C_3	C_2	C_1	C_{ext}^{21}	p	e_a^{21}	e_{ext}^{21}	GCI_{fine}^{21}
48k Straight	1.35	1.52	0.715	0.714	0.714	0.714	9.920	0.01%	0.00%	0.00%
48k CC	1.36	1.30	0.705	0.705	0.705	0.706	1.194	0.05%	0.13%	0.16%
48k 5D	1.33	1.31	0.715	0.709	0.708	0.708	8.672	0.07%	0.01%	0.01%
332k Straight	1.35	1.52	0.714	0.713	0.713	0.713	7.383	0.02%	0.00%	0.00%
332k CC	1.36	1.30	0.704	0.701	0.701	0.701	20.080	0.00%	0.00%	0.00%
332k 5D	1.33	1.31	0.714	0.706	0.704	0.704	5.193	0.26%	0.09%	0.11%
720k Straight	1.35	1.52	0.715	0.714	0.714	0.714	7.933	0.02%	0.00%	0.00%
720k CC	1.36	1.30	0.705	0.701	0.701	0.701	6.424	0.07%	0.02%	0.02%
720k 5D	1.33	1.31	0.715	0.707	0.704	0.703	4.530	0.32%	0.14%	0.17%

0.7 Beta Ratio

Similar to the 0.5 Beta ratio flowmeter, the 0.7 was not physically tested. The CFD simulations show the same general trend as the 0.5 and 0.6 flowmeters. The results of the k-ε simulations of the 0.6 beta ratio flowmeter are shown in Figure 14. However, the 0.7 beta ratio results shows negligible effect on the flowmeter at five diameters downstream of the DEOP. This is very similar to the physical data of the 0.6 beta ratio flowmeter. Table 17 shows the GCI calculations for each run, and Table 18 shows the general statistics of the uncertainty. The average uncertainty for these simulations was 0.33%. The simulation with the maximum uncertainty of 1.42% was the close coupled simulation at 48,000 Reynolds number.

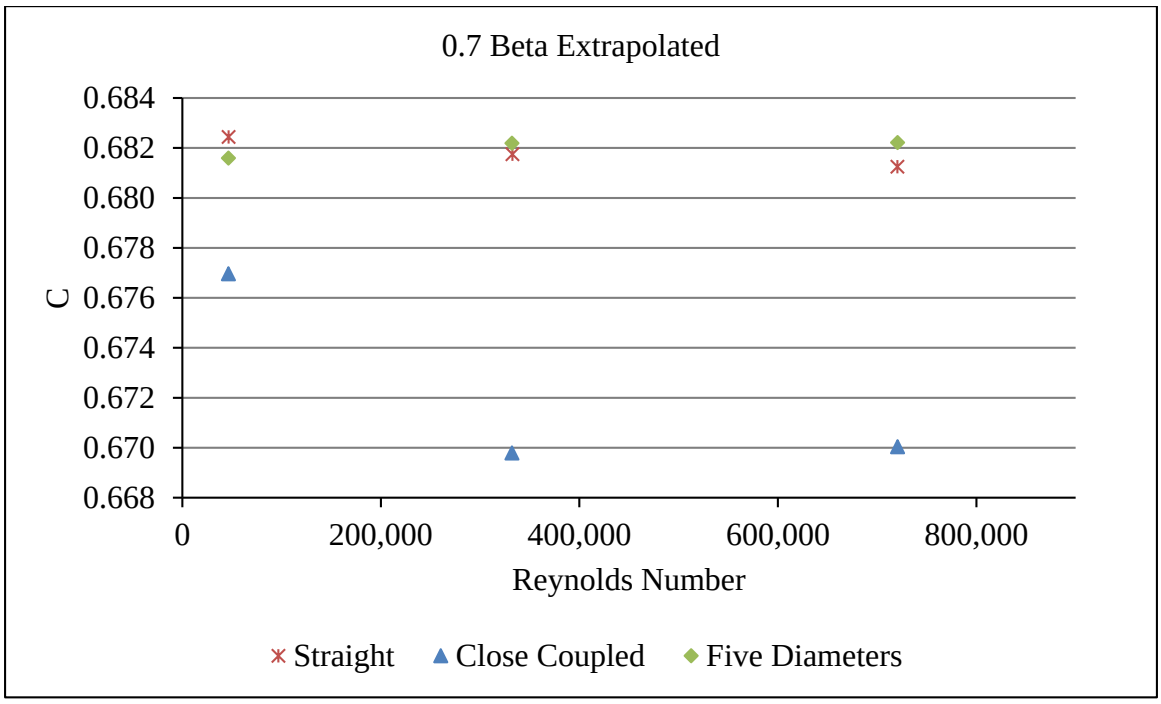

Figure 13: CFD Results 0.7 Beta Ratio Flowmeter

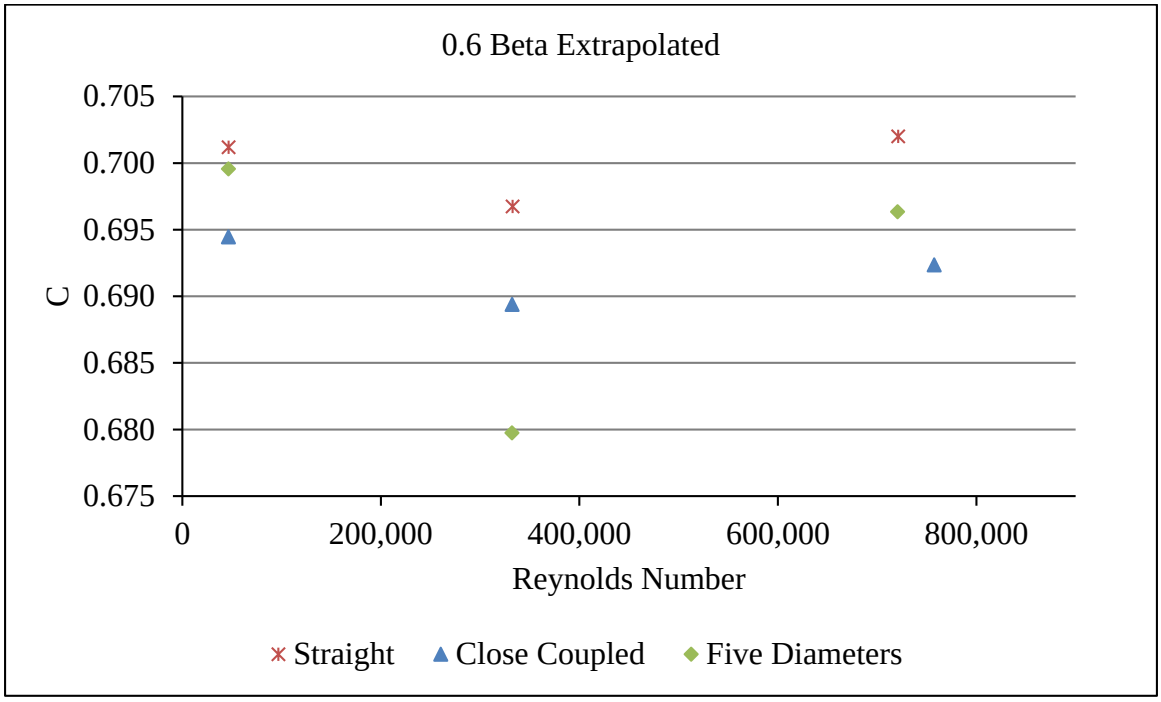

Figure 14: k-ε CFD Results 0.6 Beta Ratio Flowmeter

Table 17: Summary of GCI calculations for C for 0.5 Beta Ratio Simulations

0.7 Beta Ratio Simulations - GCI										
Simulation	r_{21}	r_{32}	C_3	C_2	C_1	C_{ext}^{21}	p	e_a^{21}	e_{ext}^{21}	GCI_{fine}^{21}
48k Straight	1.30	1.58	0.679	0.680	0.681	0.682	1.520	0.16%	0.15%	0.19%
48k CC	1.35	1.31	0.669	0.667	0.669	0.677	0.968	0.34%	1.13%	1.42%
48k 5D	1.34	1.30	0.684	0.684	0.682	0.682	4.049	0.20%	0.10%	0.13%
332k Straight	1.30	1.58	0.678	0.679	0.680	0.682	1.519	0.20%	0.20%	0.25%
332k CC	1.35	1.31	0.671	0.668	0.669	0.670	3.637	0.12%	0.07%	0.09%
332k 5D	1.34	1.30	0.685	0.684	0.683	0.682	4.611	0.22%	0.09%	0.12%
720k Straight	1.30	1.58	0.679	0.680	0.681	0.685	0.673	0.19%	0.52%	0.65%
720k CC	1.35	1.31	0.672	0.669	0.670	0.670	5.944	0.08%	0.02%	0.02%
720k 5D	1.34	1.30	0.685	0.685	0.683	0.682	6.551	0.30%	0.06%	0.08%

Table 18: Statistical Analysis for 0.7 Beta Ratio Simulations

Overall Statistical Analysis - 0.7 Beta Ratio				
	p	e_a^{21}	e_{ext}^{21}	GCI_{fine}^{21}
Average	3.275	0.20%	0.26%	0.33%
Standard Deviation	2.072	0.08%	0.34%	0.42%
Minimum	0.673	0.08%	0.02%	0.02%
Maximum	6.551	0.34%	1.13%	1.42%

Turbulence Models

A motivation for this study was to compare the performance of different turbulence models. The following section illustrates the results for each turbulence model with respect to the physical data. The mesh refinement for each geometry was the same. A near wall modeling approach was used for all simulations Figure 15 shows the CFD results of the k-ε simulations on the 0.6 beta ratio flowmeter as well as the physical data. This figure is helpful to see how the simulations compare with the actual values. The outlier of the data is the five diameter 332,000 Reynolds number simulation that has a 2.99% uncertainty.

Figure 16 compares the Elliptic Blending simulations for the 0.6 beta ratio flowmeter with the physical data. The Elliptic Blending simulations have some of the greatest uncertainties from the mesh refinement. Table 19 shows the GCI calculations for the Elliptic Blending turbulence model simulations. From this table it can be seen that many of the extrapolated values have an uncertainty of approximately 3%. Table 20 shows that the average uncertainty for all of the simulations is 1.3%.

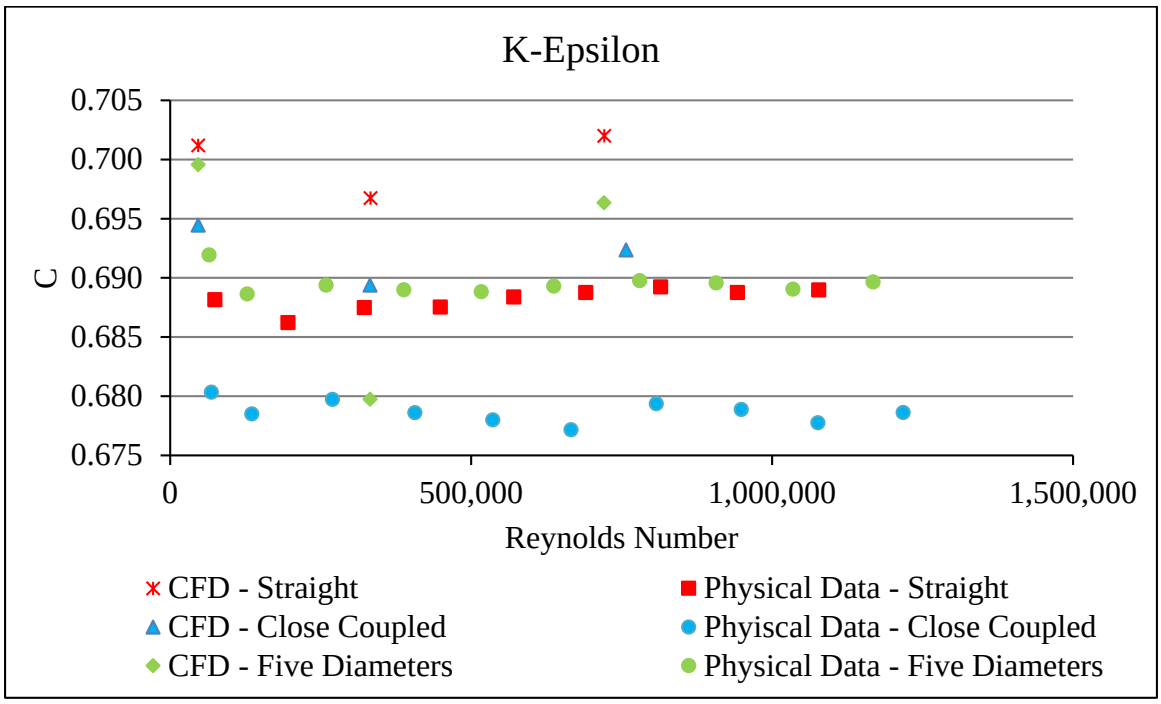

Figure 15: k-ε Model vs. Physical Results 0.6 Beta Ratio Flowmeter

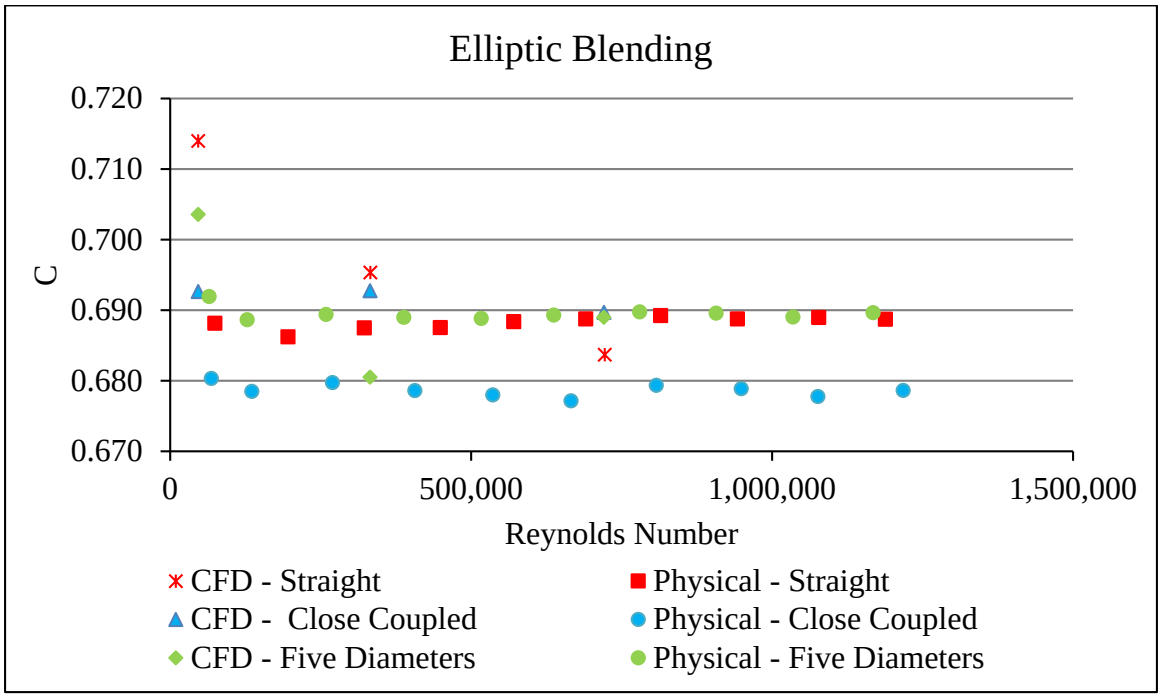

Figure 16: Elliptic Blending Model vs. Physical Results 0.6 Beta Ratio Flowmeter

Table 19: Summary of GCI Calculations for Elliptic Blending Simulations

Elliptic Blending Simulations - GCI										
Simulation	r_{21}	r_{32}	C_3	C_2	C_1	C_{ext}^{21}	p	e_a^{21}	e_{ext}^{21}	GCI_{fine}^{21}
48k Straight	1.31	1.31	0.702	0.697	0.701	0.714	0.989	0.57%	1.83%	2.33%
332k Straight	1.31	1.31	0.702	0.703	0.701	0.695	1.374	0.35%	0.79%	0.98%
720k Straight	1.31	1.31	0.701	0.703	0.701	0.684	0.403	0.28%	2.53%	3.09%
48k Close Coupled	1.31	1.31	0.698	0.700	0.698	0.693	1.081	0.27%	0.81%	1.00%
332k Close Coupled	1.31	1.31	0.693	0.693	0.693	0.693	5.677	0.04%	0.01%	0.01%
720k Close Coupled	1.31	1.31	0.693	0.692	0.692	0.690	1.374	0.12%	0.26%	0.32%
48k Five Diameters	1.30	1.30	0.708	0.704	0.704	0.704	11.899	0.03%	0.00%	0.00%
332k Five Diameters	1.30	1.30	0.704	0.701	0.697	0.681	0.743	0.52%	2.46%	3.00%
720k Five Diameters	1.30	1.30	0.703	0.701	0.694	0.689	3.009	0.92%	0.76%	0.95%

Table 20: Statistical Analysis for Elliptic Blending Simulations

Overall Statistical Analysis - Elliptic Blending				
	p	e_a^{21}	e_{ext}^{21}	GCI_{fine}^{21}
Average	2.950	0.34%	1.05%	1.30%
Standard Deviation	3.515	0.27%	0.93%	1.14%
Minimum	0.403	0.03%	0.00%	0.00%
Maximum	11.899	0.92%	2.53%	3.09%

CFD Flow Visualizations

Figure 18 - 71 show the streamlines and the centerline velocity of the various simulations on the 0.6 beta ratio flowmeter. Figure 18 -21 are in in the text and Figure 24 - 71 are located in Appendices A - C. The figures are organized into three different groups; the straight pipe simulations, the close coupled simulations, and finally the simulations at five diameters. For each of these sections, the streamlines and centerline velocities are shown for each turbulence model at the three different flow velocities.

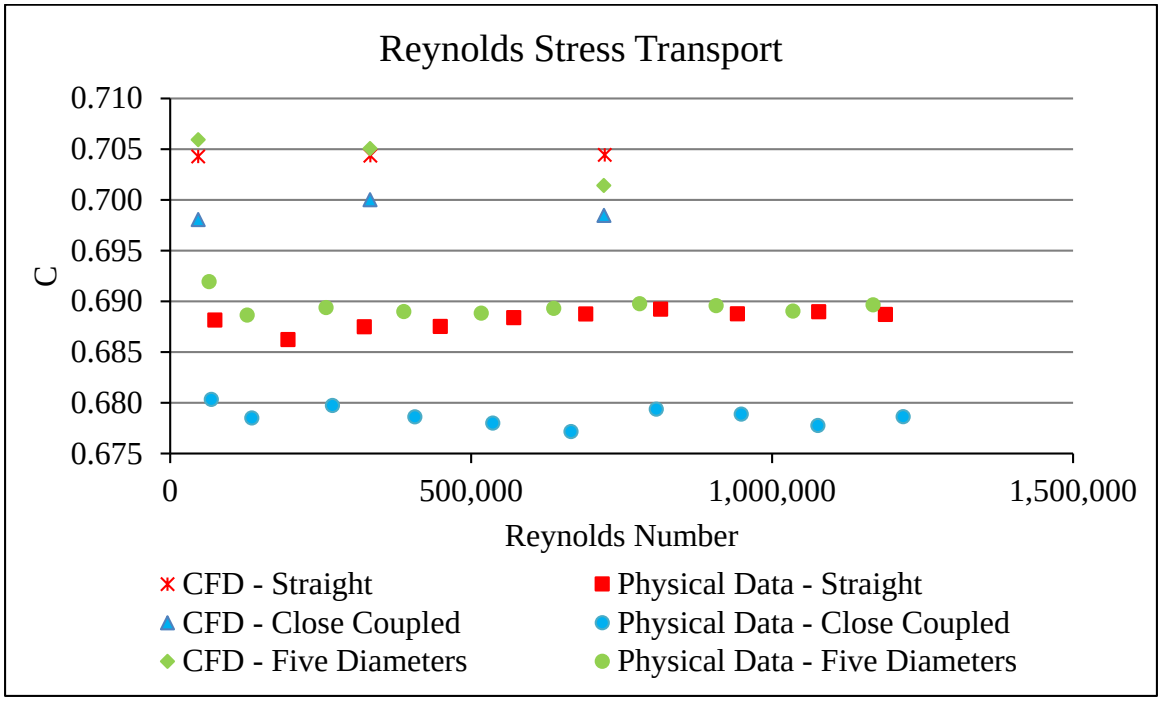

Figure 17: Reynolds Stress Transport Model vs. Physical Results 0.6 Beta Ratio Flowmeter

Straight Pipe Simulations

Figure 18 and Figure 19 in the text and Figure 24 - 39 in Appendix A show the straight pipe simulations that were conducted on the finest meshes. All have a fully developed uniform inlet flow profile. The main difference that can be noticed from these figures is the length of the recirculation zone downstream of the wedge constriction. Table 21 shows the length of the recirculation zone downstream of the constriction of the wedge flow meter for the various simulations in terms of step height or in other words the length of the recirculation zone was normalized by the height of the wedge constriction.

These values were calculated from the simulations with the finest mesh. The recirculation length was found by observing the axial velocity along the center line of the pipe one inch from the pipe wall. The recirculation length was then taken as the distance downstream of the wedge flow constrictions to the point in which the axial velocity changed from a negative velocity to a positive velocity.

Table 21: Recirculation Lengths Downstream of Wedge Constriction

Turbulence Model	Flow Velocity (ft/s)	Recirculation Length (Step Height)		
		Straight	Close Coupled	Five Diameters
k-ε	0.7	24.07	14.37	23.56
	5	24.30	14.56	23.34
	11	24.35	14.89	23.48
Elliptic Blending	0.7	23.97	12.69	20.94
	5	24.30	18.27	25.66
	11	24.30	18.42	25.89
Reynold Stress Transport	0.7	20.94	11.66	20.25
	5	21.16	11.94	20.41
	11	21.09	12.07	20.03

Figure 18 in the text and Figure 24 and 25 in Appendix A are the straight pipe simulations that were run with the k-ε turbulence model. Figure 26 - 28 show the streamlines and Figure 37- 39 show the centerline velocity contour for the Reynolds Stress Transport turbulence model. Figure 29 -31 and Figure 34 - 36 are the results for the Elliptic Blending turbulence model. The Reynolds Stress Transport model has the shortest recirculation zone of the three turbulence models. This could explain the overall higher coefficient derived from these simulations. Figure 18 and Figure 19 as shown

below show the straight pipe simulation with a flow velocity of 11 *ft/s* simulated with the k-ε turbulence model.

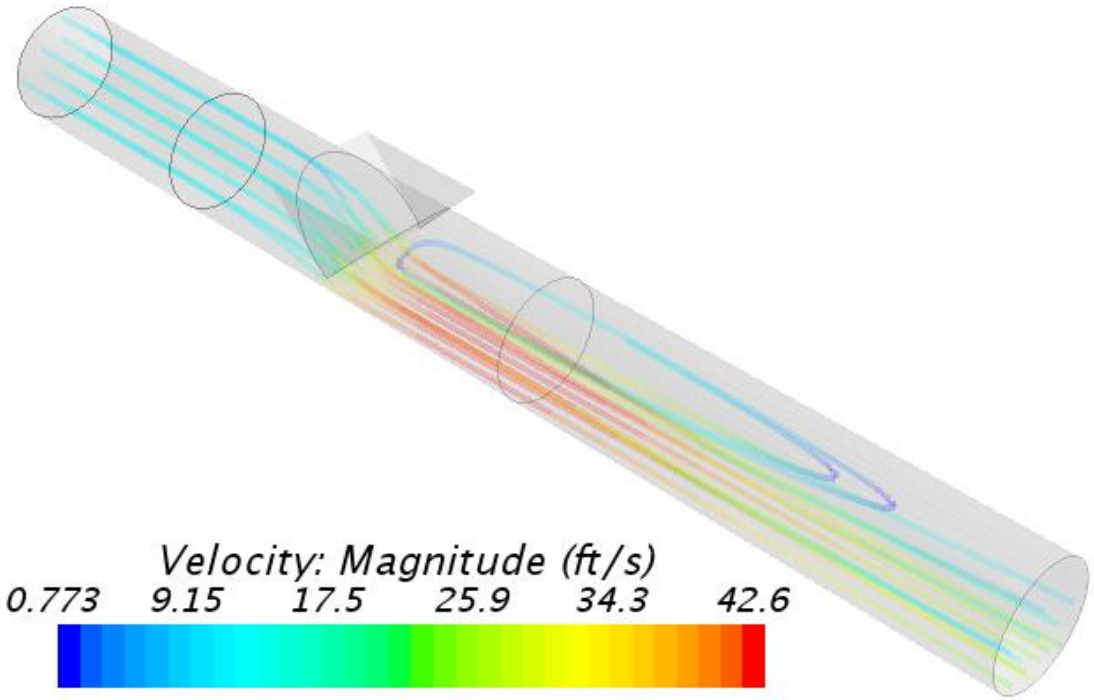

Figure 18: Streamlines, 11 *ft/s* Straight Pipe k-ε

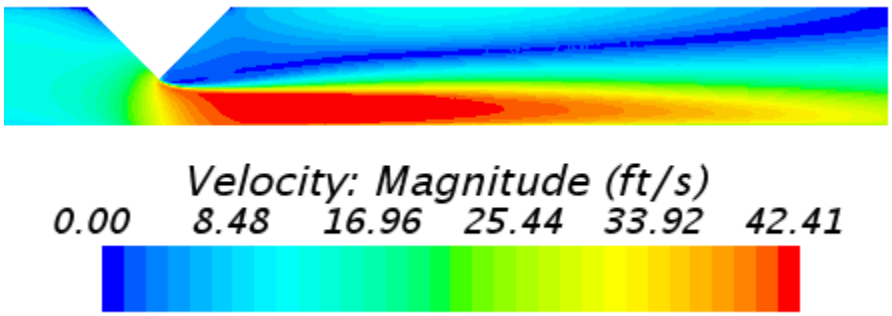

Figure 19: Centerline Velocity Magnitude, 11 *ft/s* Straight Pipe k-ε

Close Coupled Simulations

Figure 22 and Figure 20 in the text, and Figure 40 - 55 in Appendix B show the streamlines and centerline velocities for the finest mesh for each of the flow velocities and each of the turbulence models for the closed coupled simulations. These simulations have a fully developed flow profile as the inlet to the simulation. Immediately downstream of the DEOP is the wedge flowmeter. The streamlines show the non-uniform flow profile as it enters the wedge flowmeter. Figure 22 in the text and, Figure 40 and Figure 41 in Appendix B, show the streamlines of the k-ε turbulence model. Figure 20 in the text and Figure 32 and Figure 33 in Appendix B, show the centerline velocities of the k-ε turbulence model. Figure 42-44 and Figure 53 - 55 in Appendix B show the results of the Reynolds Stress Transport turbulence model. Figure 45 - 47 in Appendix B show the streamlines and Figure 50 - 52 in Appendix B show the centerline velocity of the Elliptic Blending turbulence model. The swirling effect is still partially visible downstream of the flow constriction for most of the simulations, with the Reynolds Stress Transport turbulence model displaying the least dissipated swirl downstream of the flow constriction. Figure 22 and Figure 20 shown below display the streamlines for the 11 *ft/s* close coupled k-ε simulation.

Five Diameters Downstream Simulations

Figure 23 and Figure 21 in the text and Figure 56 -71 in Appendix C show the streamlines and centerline velocities for the all the simulations ran with the flowmeter at five diameters downstream of the DEOP. Figure 23 and Figure 21 in the text and Figure 56 and 57 as well as Figure 64 and 65 in Appendix C are the simulations that used the k-ε

turbulence model. Figure 58 - 60 and Figure 69 - 71 show the simulations that used the Reynolds Stress Transport turbulence model. Figure 61 - 63 and Figure 66 - 68 show the simulations that used the Elliptic Blending turbulence model. The Reynolds Stress Transport model shows the least dissipation of the swirling flow generated from the DEOP and the shortest recirculation zone of the three turbulence models used. Figure 23 and Figure 21 shown below displays the streamlines of the simulation with a flow velocity of 11 *ft/s* with the wedge flowmeter located at five diameters downstream of the DEOP with the k-ε turbulence model.

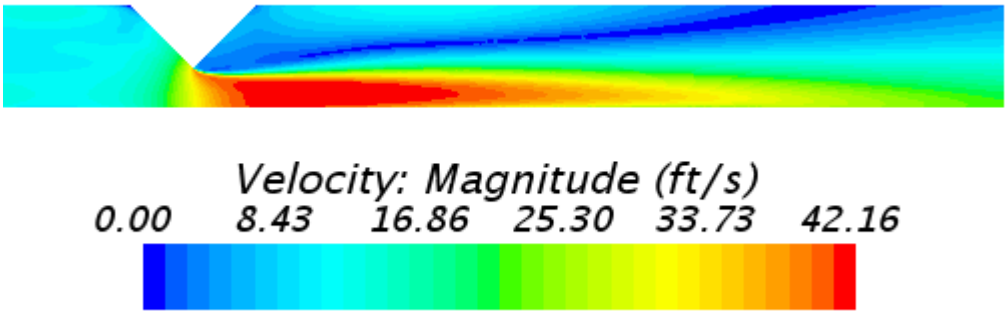

Figure 20: Centerline Velocity Magnitude Contour, 11 *ft/s*, Close Coupled, k-ε

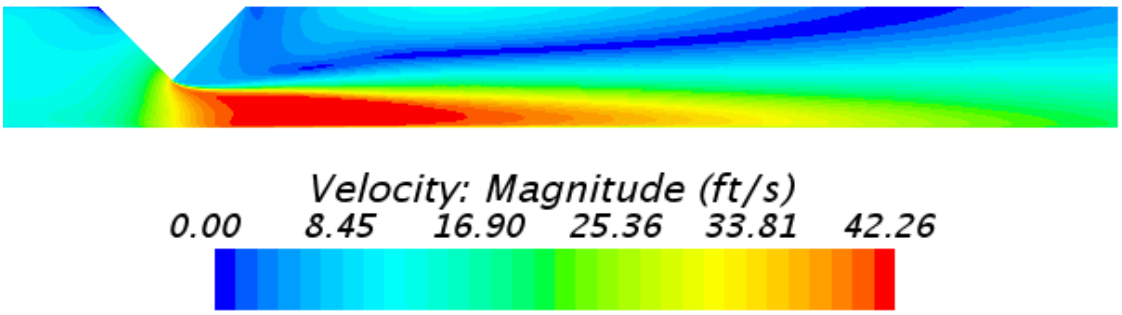

Figure 21: Centerline Velocity Magnitude Contour, 11 *ft/s*, Five Diameters, k-ε

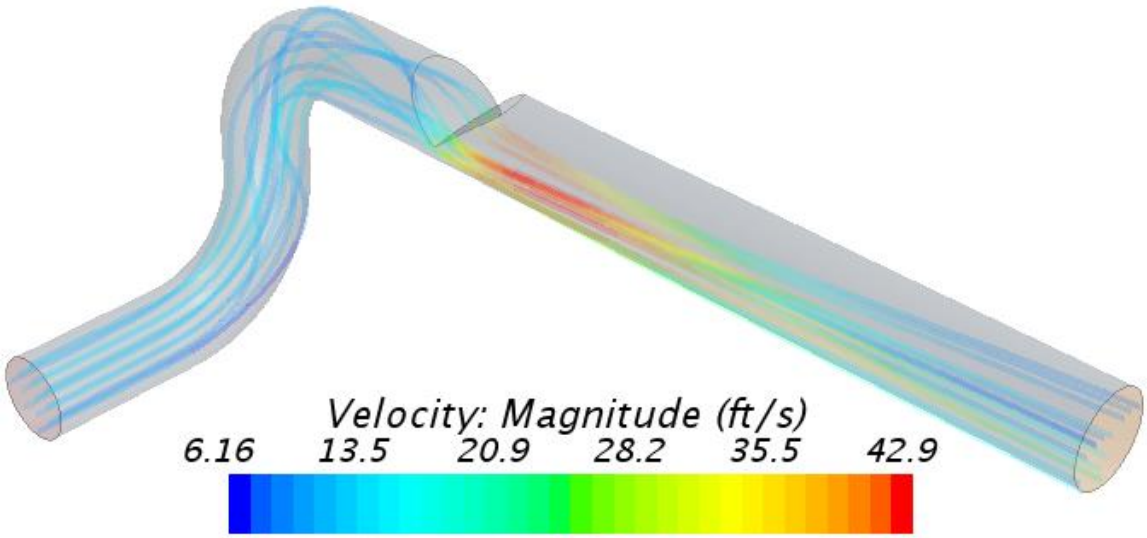

Figure 22: Streamlines, 11 *ft/s*, Close Coupled, k-ε

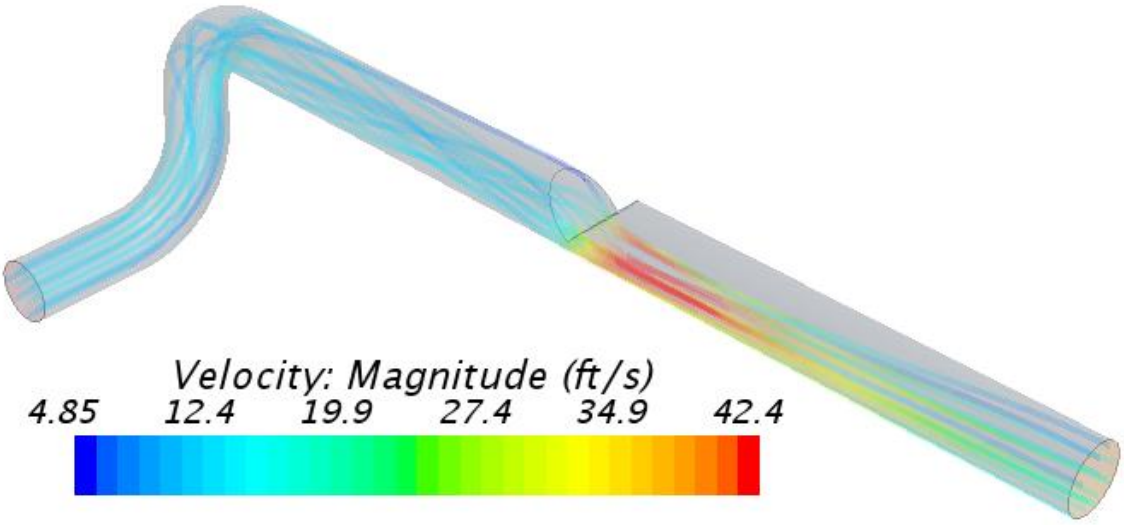

Figure 23: Streamlines, 11 *ft/s*, Five Diameters, k-ε

CHAPTER VII

DISCUSSION AND CONCLUSION

Flowmeter Location

Not only does the location of the flowmeter downstream of a flow disturbance affect the performance of the flow meter, but the orientation of the flow meter also needs to be taken into effect. If only the CFD results were considered in this study, the general trend of meter performance would have given a good representation of the physical data. Although the CFD did not produce exactly the same results as the physical data, the CFD results closely predicted the shift in C when the flowmeter was close coupled to the DEOP. The CFD predicted a decrease in the flowmeter's coefficient due to the installation downstream of the DEOP.

Also, the orientation of the flowmeter affects the performance of the flowmeter. When the flowmeter was close coupled to the DEOP, installing the flowmeter with the pressure taps out of plane with the DEOP, the effect of the DEOP was greatly reduced as compared to when the flowmeter in plane with the second elbow in the DEOP. This is assumed to be due to the distorted flow profile exiting the elbow. The CFD predicted that at five diameters the effect of the DEOP would be less than at zero diameters. The physical data showed that the effect was negligible at five diameters. The orientation of the flowmeter at five diameters did not have an effect on the coefficient of the meter.

Table 22 and Table 23 show the swirl angles that were calculated from the finest mesh simulations. The swirl angle was calculated by taking the average of the arctangent between the axial velocity vector and the resultant tangential velocity vector at each cell a

plane perpendicular to the direction of axial flow. Table 22 are the swirl angles calculated with no flowmeter installed downstream of the DEOP. According to experimental data taken by D.M. Halsey [12] six diameters downstream of a DEOP the swirl angle is 9.71°. This value is consistent with the values in Table 22. The discrepancies could be due to the slight change in geometry, as the simulations replicated the geometry used in the laboratory where a 5 in straight section separated the two elbows. Also in Halsey's experiment smooth walled PVC pipes were used. The trends with Reynolds number and turbulence models can be observed in this table. At five diameters, the trends are fairly consistent with Reynolds number. However, at zero diameters, the trend is not clear. This could be due to the slower velocity allowing the tangential velocities to have a greater influence over the axial velocity. Turbulence model also effects the swirl angle as expected.

Table 22: Swirl Angle Downstream of DEOP with no Flowmeter

Swirl Angle (No Flowmeter)				
Reynolds Number	Location Downstream	Swirl Angle (degrees)		
		k-ε	Elliptic Blending	Reynold Stress Transport
48k	0D	16.68	17.07	20.04
	5D	8.40	8.50	8.18
332k	0D	13.86	14.26	15.98
	5D	9.16	9.26	9.63
720k	0D	14.25	13.86	15.36
	5D	9.22	9.37	9.81

Table 23 displays the swirl angles at the inlet of the flowmeter when the flowmeter is located five diameters downstream of the DEOP. The laboratory results

showed negligible effect on the flowmeter when at this location. Therefore, it could be interpreted that if the swirl angle is less than approximately 8°, negligible effects will be observed. The results of Table 23 are similar to Table 22. The discrepancies could be due to the effect of the flowmeter's constriction on the flow profile.

Table 23: Swirl Angle with Flowmeter at Five Diameters

Swirl Angle with Flowmeter at Five Diameters				
Reynolds Number	Location Downstream	Swirl Angle (degrees)		
		k-ε	Elliptic Blending	Reynold Stress Transport
48k	0D	16.71	24.54	20.13
	5D	8.45	11.92	9.93
332k	0D	15.17	14.40	16.17
	5D	9.27	9.33	9.68
720k	0D	14.35	14.01	15.06
	5D	9.35	9.47	9.87

This data can be very useful for those who desire to use a wedge flowmeter in close proximity to a DEOP. One such example of an area that could benefit from this would be in the oil industry on an off shore oil rig. This is a situation that the pipe network has a limited footprint that could benefit from having a reduced upstream pipe length without the added head loss due to a flow conditioner. Also, by rotating the flowmeter the coefficient for the flowmeter would be higher, and thus leading to less energy loss in the flow.

The effect of swirling flow on different beta ratio wedge flowmeters was investigated in this study by simulating a 0.5, 0.6, and a 0.7 beta ratio wedge flowmeter.

The CFD results show that for the 0.5 beta ratio flowmeter there was a percent change in the coefficient of 1.5 percent when the flow meter is closed coupled to the DEOP. The close coupled 0.7 beta ratio flowmeter produced similar results of a 1.4 percent change in the flowmeters coefficient. These percent changes are too close to be able to assume a trend in the effect the beta ratio has on the flow meter. The percent change of the coefficient at five diameters downstream of the DEOP for the 0.5 beta ratio flow meter was 0.72 percent, whereas for the 0.7 beta ratio flowmeter the percent change was 0.03percent. Based upon these results the trend seems to be that the larger beta ratio flowmeter is affected less by swirl. A study done by G.L. Morrison et al. [13] investigated axisymmetric flow distortion and swirl effects on orifice flowmeters. They found that as the beta ratio was increased the orifice flowmeter was more sensitive to the disturbance. However, the sensitivity to swirl decreased with increasing beta ratio from 0.43 to 0.65 and then the sensitivity increased rapidly when the beta ratio was greater than 0.65. More testing would be required to ensure the relationship between swirl and beta ratio for wedge flowmeters.

Turbulence Models

Three turbulence model were used to compare which would best model the highly complex swirling turbulent flow that occurs from a DEOP. Although the geometry of the flow is simple the flow inside of it is not. The DEOP causes a complex swirling flow to occur and the constriction in the wedge flowmeter causes separation to occur with a large recirculating zone downstream. These types of flows are difficult to model, and therefore the k-ε, the Elliptic Blending, and the Reynolds Stress Transport turbulence models were used for comparison.

Each turbulence model provided slightly different results for similar simulations. The Reynolds Stress Transport turbulence model had the shortest recirculation zone out of the three but had the least dissipation of swirl after the flow constriction. The Elliptic Blending turbulence model performed very similar to the k-ε model, which could be expected due to the fact that it is a derivative of the k-ε turbulence model. The Elliptic Blending is computationally more expensive than the k-ε and therefore it is less desirable to use over the k-ε model if the results are similar. The turbulence model that most closely matched the physical data was the k-ε turbulence model. This turbulence model is the least computationally expensive out of the three, having the least number of equations to solve.

REFERENCES

[1] WedgeType Flow Meter Data Sheet, 2016, Primary Flow Signal, Cranston, RI.

[2] Lipták Béla G., *Flow measurement*. Radnor, Penn.: Chilton Book, 1993.

[3] Reader-Harris,M. (n.d.). Orifice Plates and Venturi Tubes.

[4] Measurement of fluid flow by means of pressure differential devices inserted in circular cross-section conduits running full. ISO 5167. Geneva Switzerland : ISO.

[5] Yoon, J.Y., Sung, N.W., Lee, C.H., 2007, "Discharge Coefficient Equation of a Segmental Wedge Flowmeter," Journal of Process Mechanical Engineering, **222**(Part E), pp. 79-83.

[6] Hilgenstock, A. and Ernst R., 1996, "Analysis of installation effects by means of computational fluid dynamics -CFD vs experiments?" Flow Measurement and Instrumentation, **7**(3/4), pp. 161-171.

[7] Gibson, J. and Reader-Harris, R., 2006, "Swirling Flow Through Venturi Tubes of Convergent Angle 10.5° and 21°," *2006 ASME Joint U.S. – European Fluids Engineering Summer Meeting,* 2006, pp. 953-962.

[8] Banchhor, P.K., Singh, S.N., Seshadri, V., Gandhi, B.K., 2002, "Performance Characteristics of Wedge Flowmeter Using CFD," Computational Fluid Dynamics Journal, **11**(3), pp. 279-284.

[9]CD-Adapco, STAR-CCM+ version 10.06.009, Users Manual.

[10] Shih, T.H., 1994," A New K-epsilon Eddy Viscosity Model for High Reynolds Number Turbulent Flows: Model Development and Validation," NASA-TM-106721, NASA Lewis Research Center, Cleveland, OH, United States

[11] Celik, I., Ghia, U., Roache, P., Freitas, C., Coleman, H., and Raad, P., "Procedure of Estimation and Reporting of Uncertainty Due to Discretization in CFD Applications*," Journal of Fluid Mechanics*, Vol. 130, No. 7, 2008.

[12] D.M. Halsey, 1986, "The character of swirl in turbulent pipe flow with reference to its effect on flowmeters" Ph.D. thesis, Department of Fluid engineering and Instrumentation, Cranfield Institute of Technology.

[13] G.L. Morrison, J.Hauglie, and R. E. DeOtte, Jr, 1995, "Beta ratio, axisymmetric flow distortion and swirl effects upon orifice flow meters," Flow Meas. Instrum., **6**(3), pp.207-216.

APPENDICES

Appendix A: Straight Pipe CFD Flow Visualizations

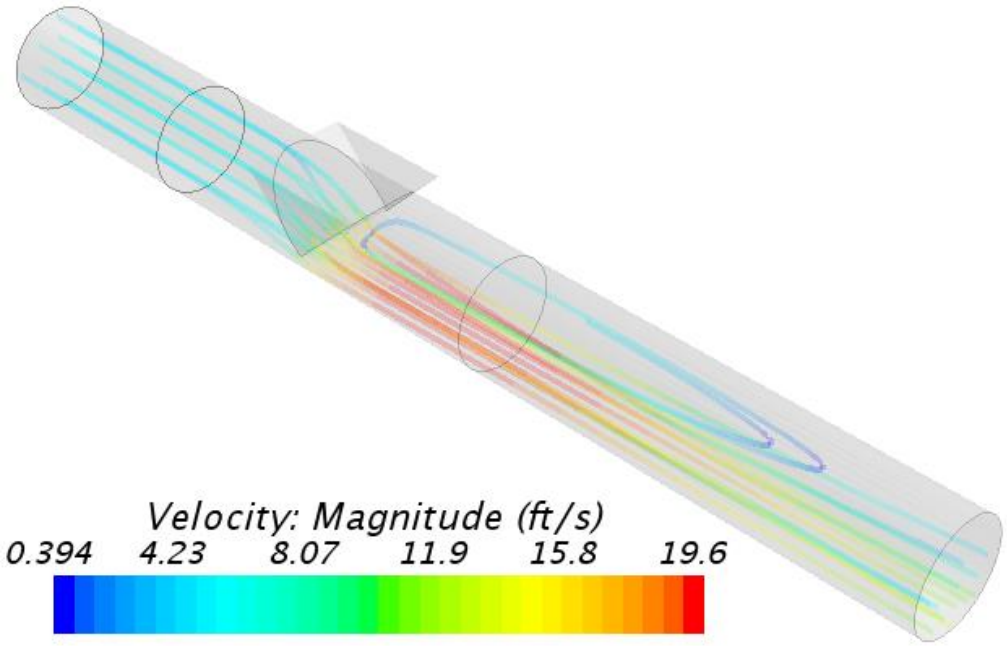

Figure 24: Streamlines, 5 *ft/s* Straight Pipe k-ε

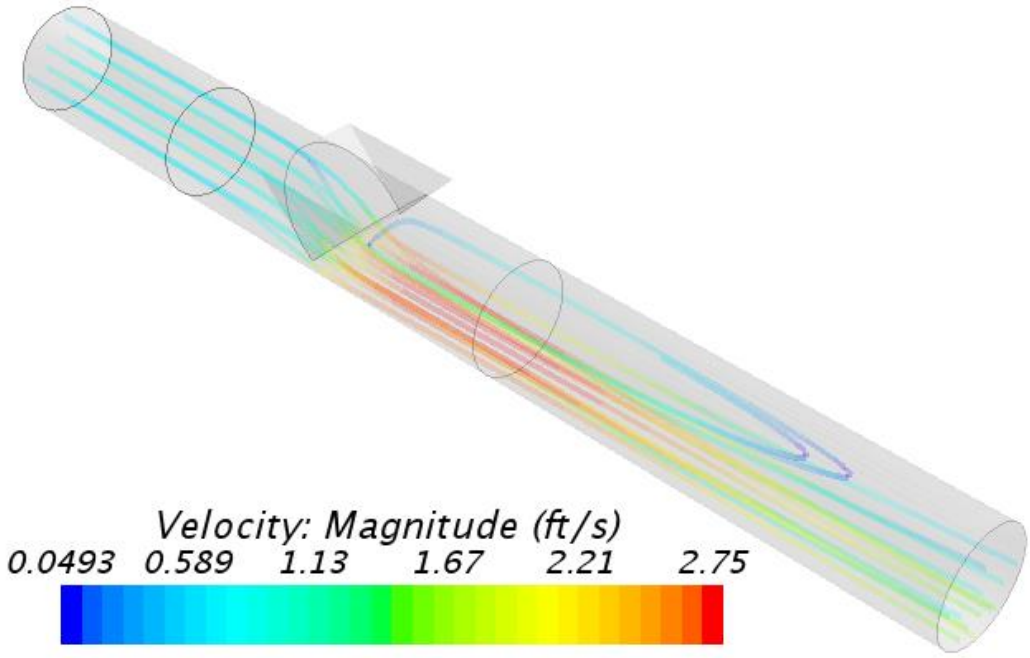

Figure 25: Streamlines, 0.7 *ft/s* Straight Pipe k-ε

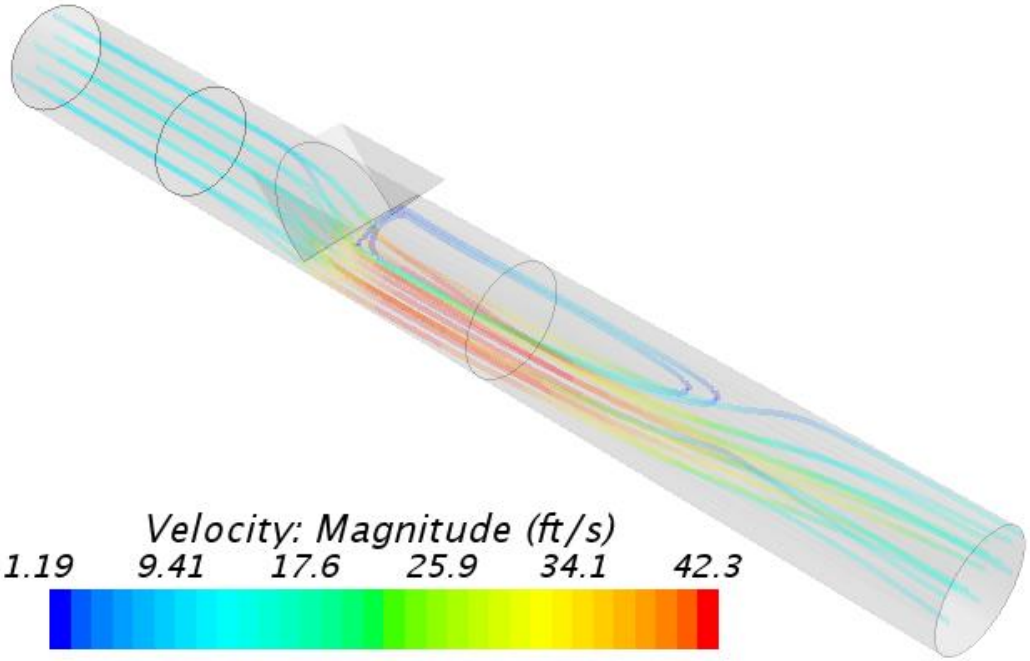

Figure 26: Streamlines, 11 *ft/s*, Straight Pipe, Reynolds Stress Transport

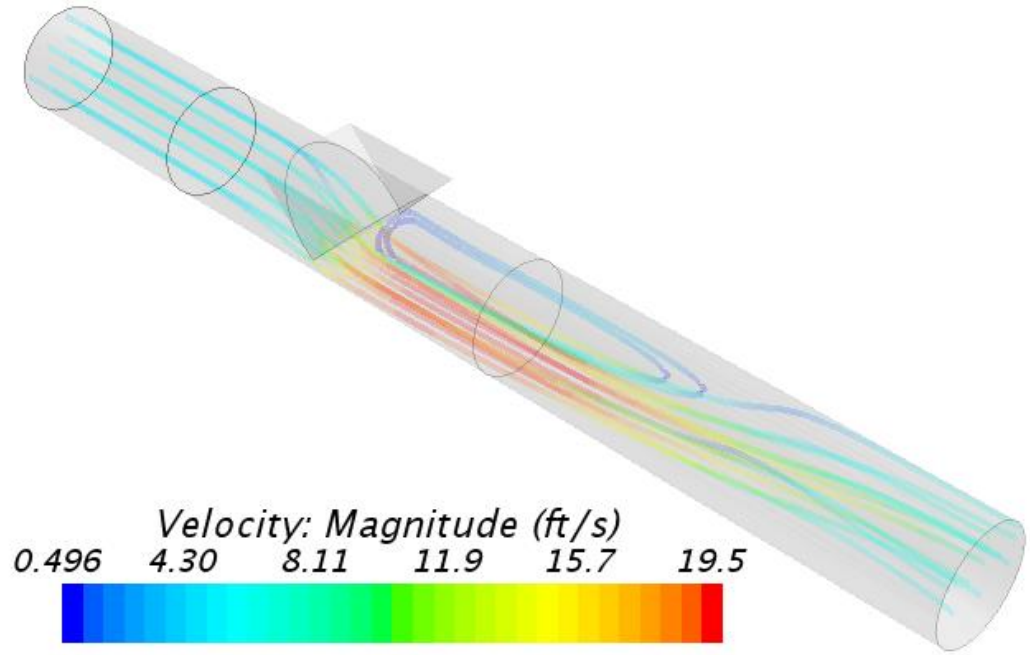

Figure 27: Streamlines, 5 *ft/s*, Straight Pipe, Reynolds Stress Transport

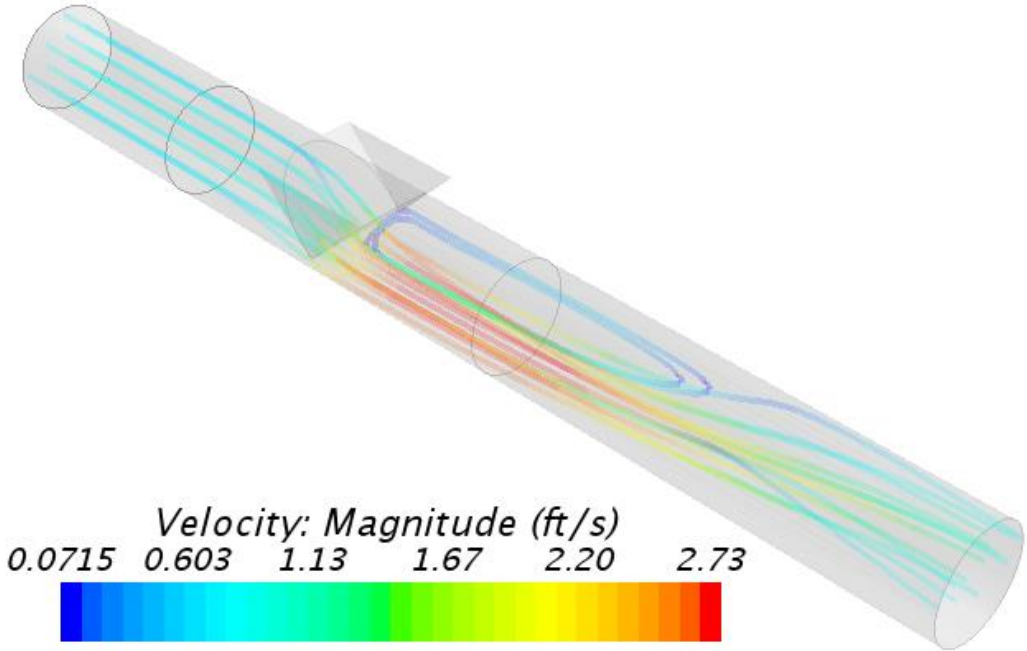

Figure 28: Streamlines, 0.7 *ft/s*, Straight Pipe, Reynolds Stress Transport

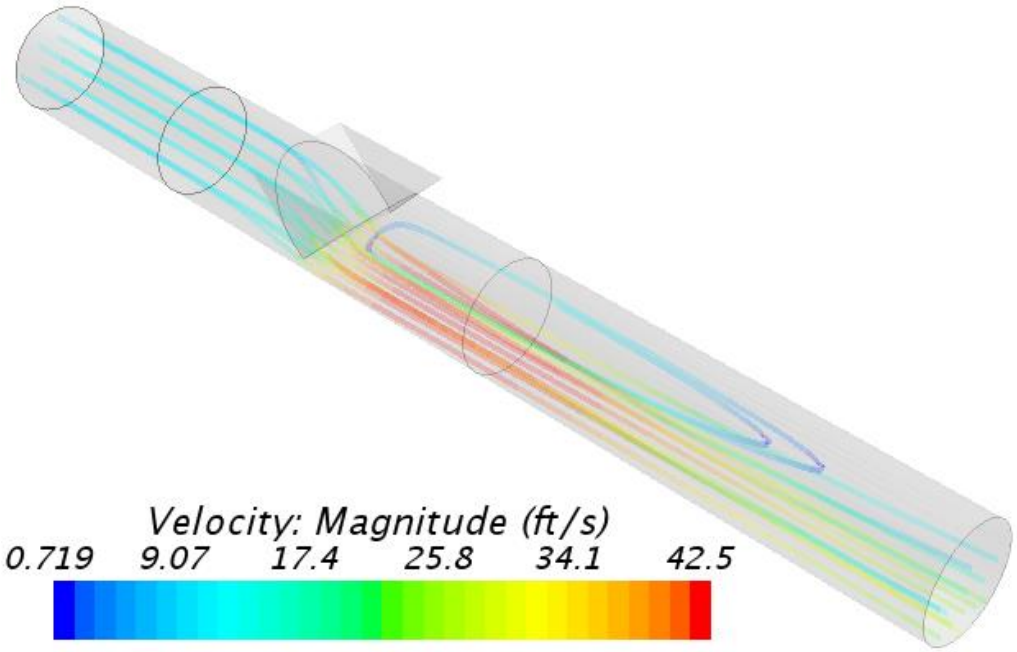

Figure 29: Streamlines, 11 *ft/s*, Straight Pipe, Elliptic Blending

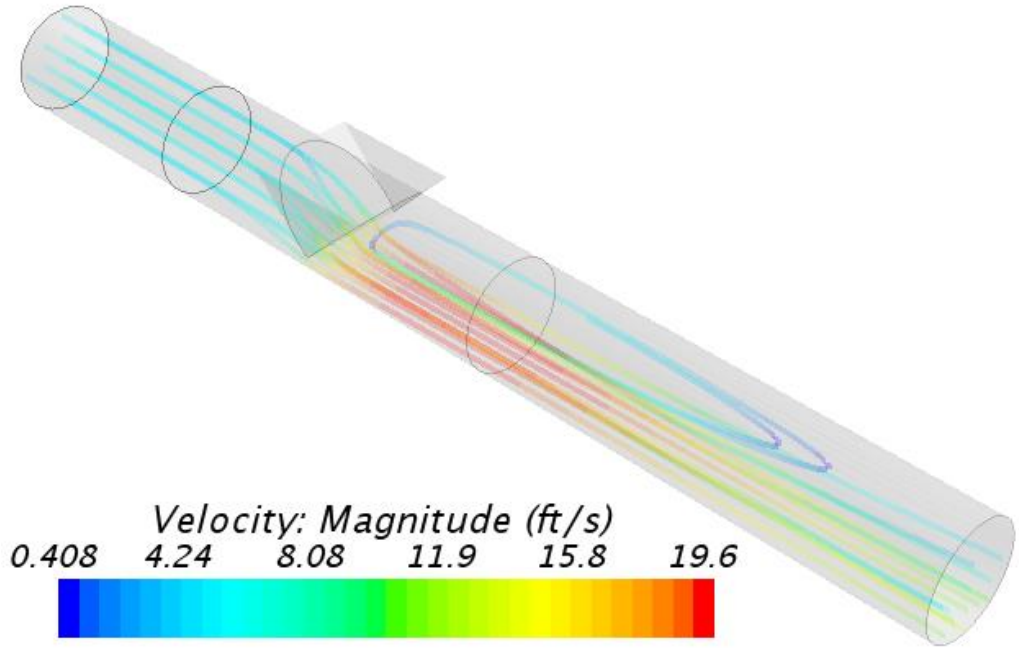

Figure 30: Streamlines, 5*ft/s*, Straight Pipe, Elliptic Blending

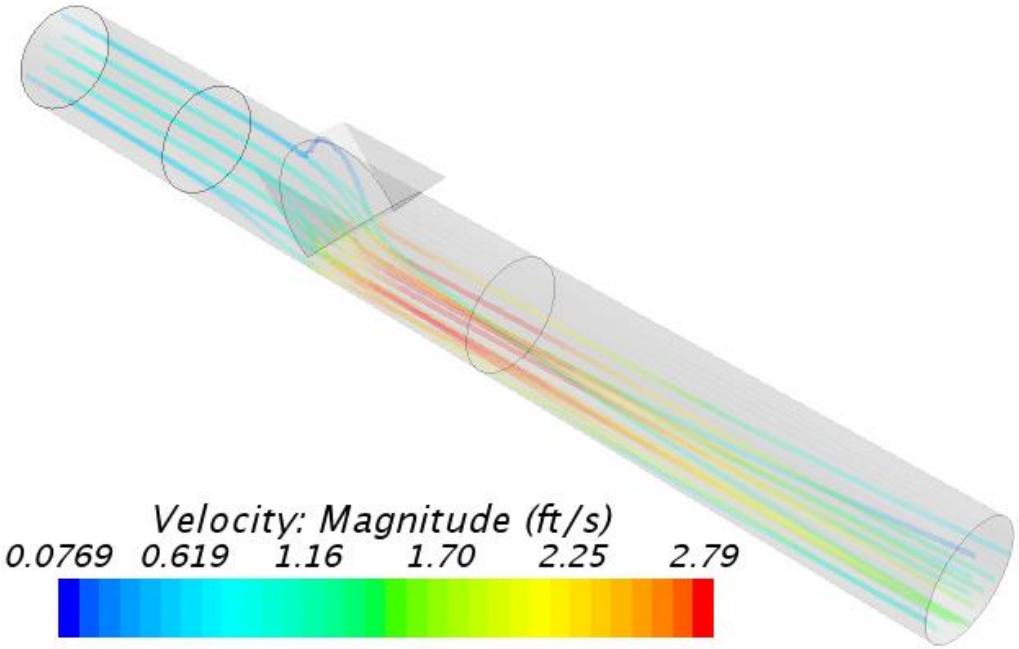

Figure 31: Streamlines, 0.7 *ft/s*, Straight Pipe, Elliptic Blending

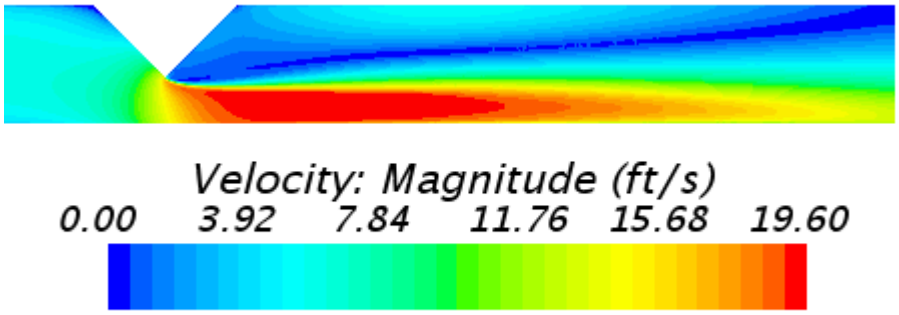

Figure 32: Centerline Velocity Magnitude Contour, 5 *ft/s*, Straight Pipe, k-ε

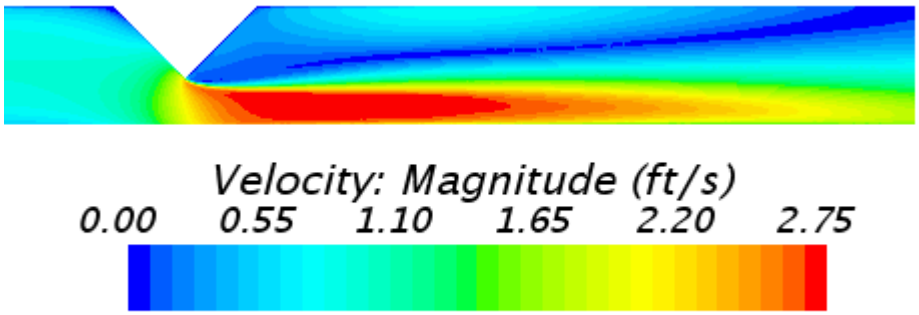

Figure 33: Centerline Velocity Magnitude Contour, 0.7 *ft/s*, Straight Pipe, k-ε

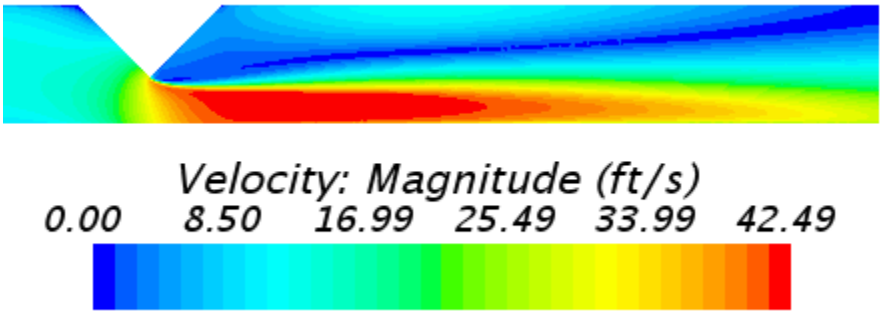

Figure 34: Centerline Velocity Magnitude Contour, 11 *ft/s*, Straight Pipe, Elliptic Blending

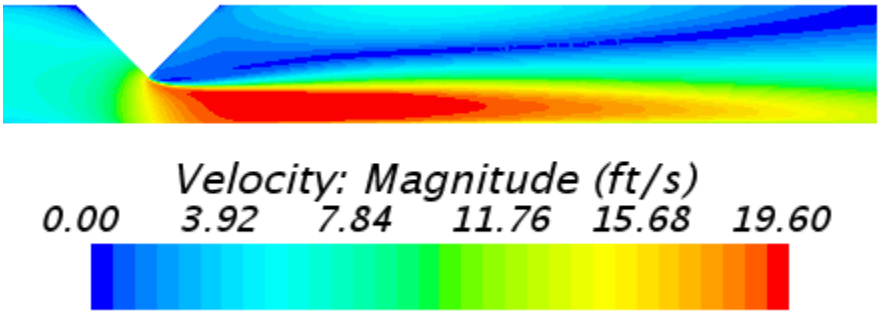

Figure 35: Centerline Velocity Magnitude Contour, 5 *ft/s*, Straight Pipe, Elliptic Blending

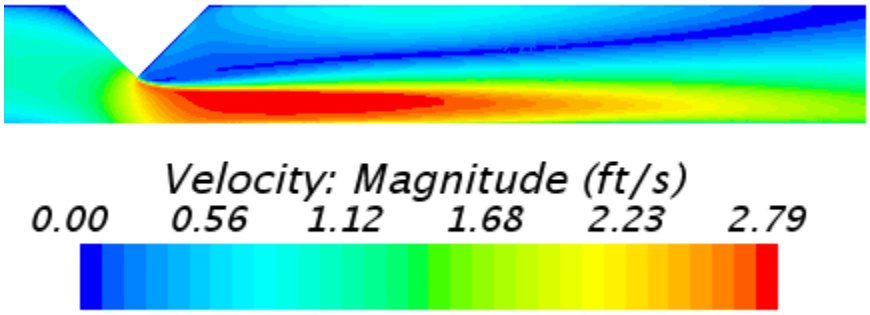

Figure 36: Centerline Velocity Magnitude Contour, 0.7 *ft/s*, Straight Pipe, Elliptic Blending

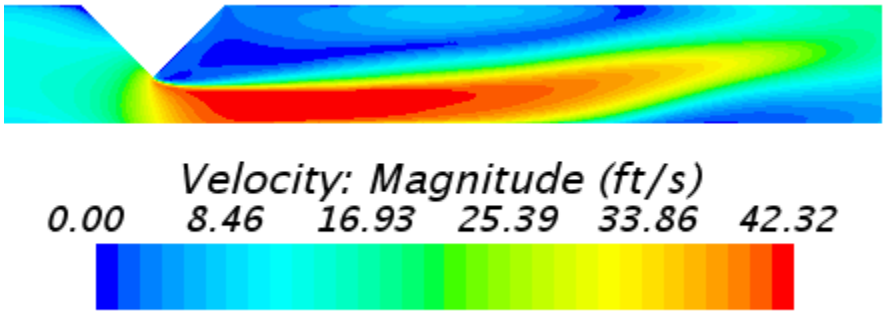

Figure 37: Centerline Velocity Magnitude Contour, 11 *ft/s*, Straight Pipe, Reynold Stress Transport

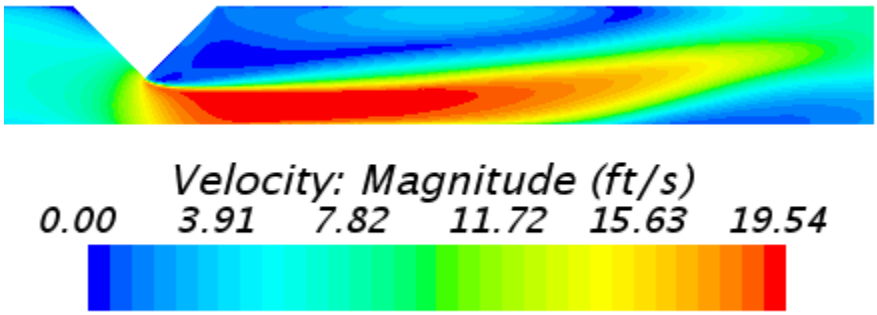

Figure 38: Centerline Velocity Magnitude Contour, 5 *ft/s*, Straight Pipe, Reynold Stress Transport

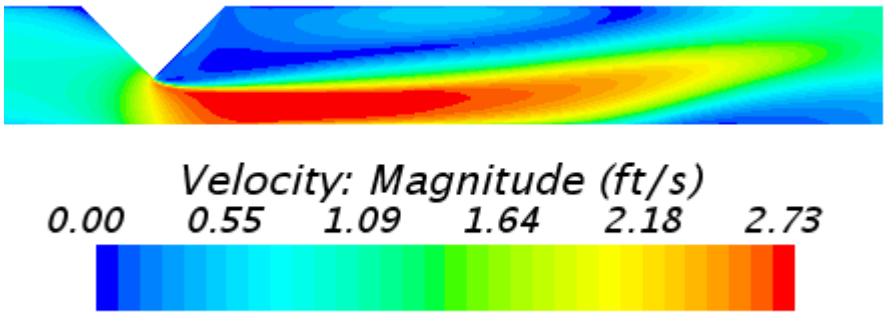

Figure 39: Centerline Velocity Magnitude Contour, 0.7 *ft/s*, Straight Pipe, Reynold Stress Transport

Appendix B: Close Coupled CFD Flow Visualizations

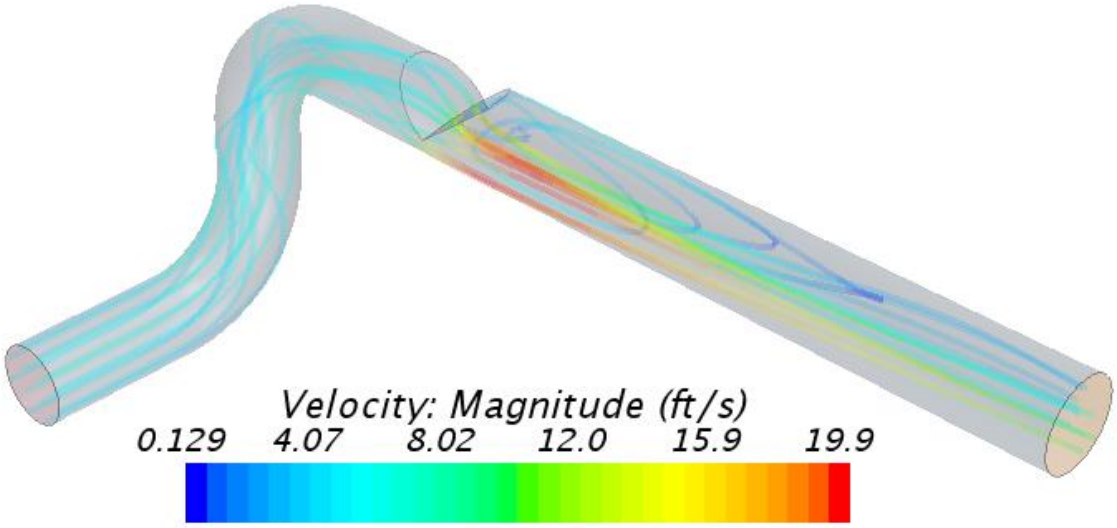

Figure 40: Streamlines, 5 *ft/s*, Close Coupled, k-ε

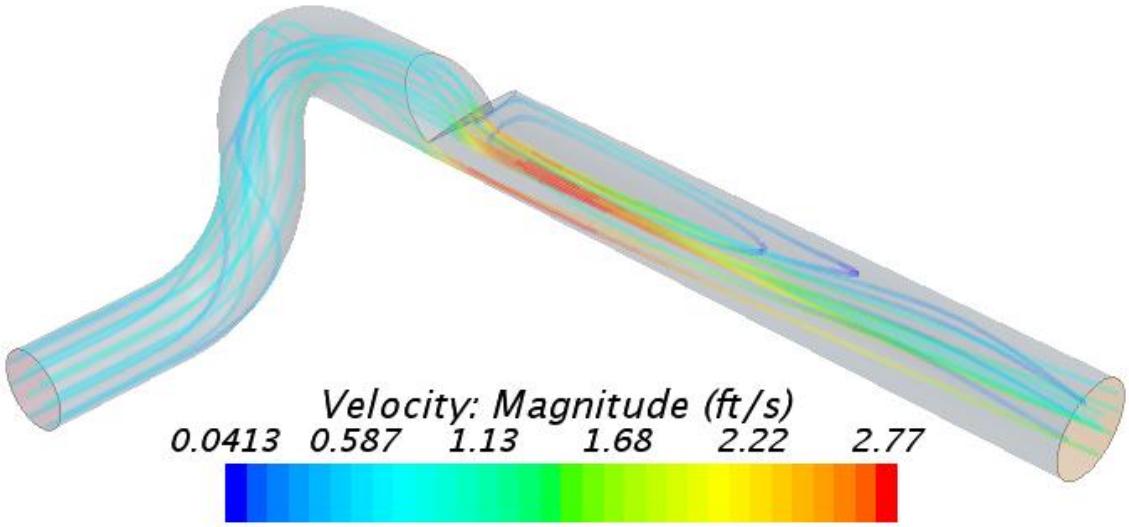

Figure 41: Streamlines, 0.7 *ft/s*, Close Coupled, k-ε

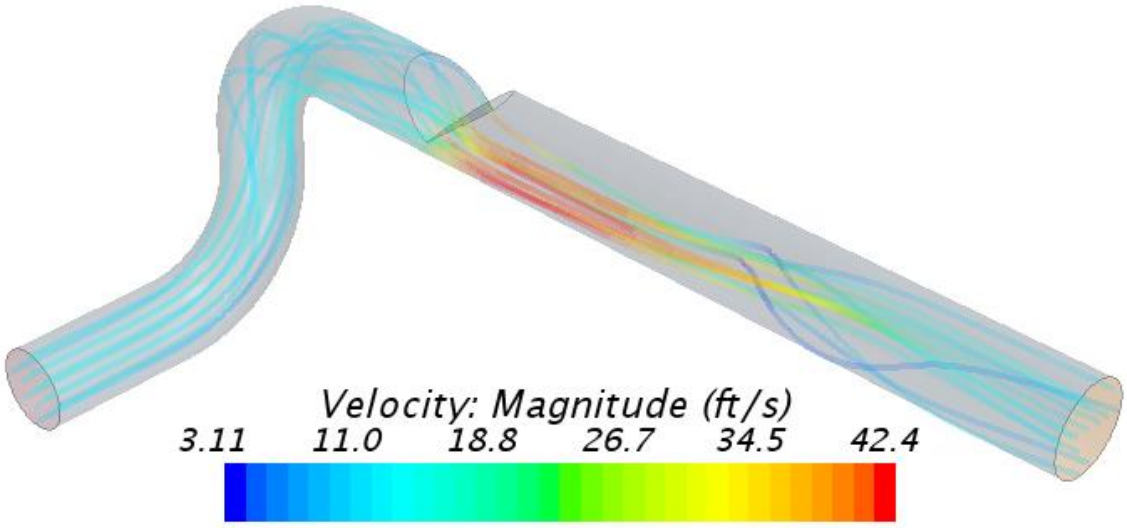

Figure 42: Streamlines, 11 *ft/s*, Close Coupled, Reynold Stress Transport

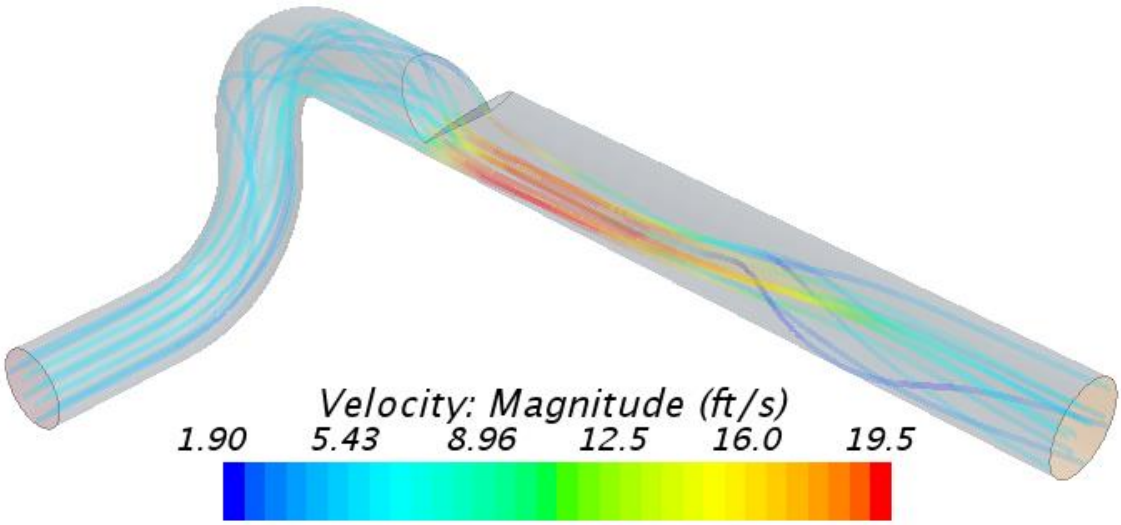

Figure 43: Streamlines, 5*ft/s*, Close Coupled, Reynold Stress Transport

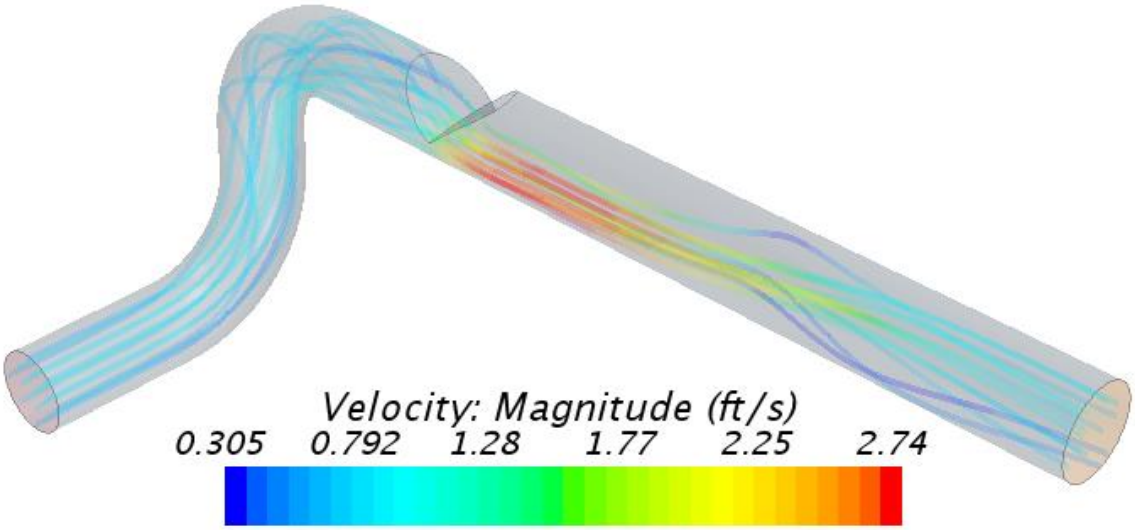

Figure 44: Streamlines, 0.7 *ft/s*, Close Coupled, Reynolds Stress Transport

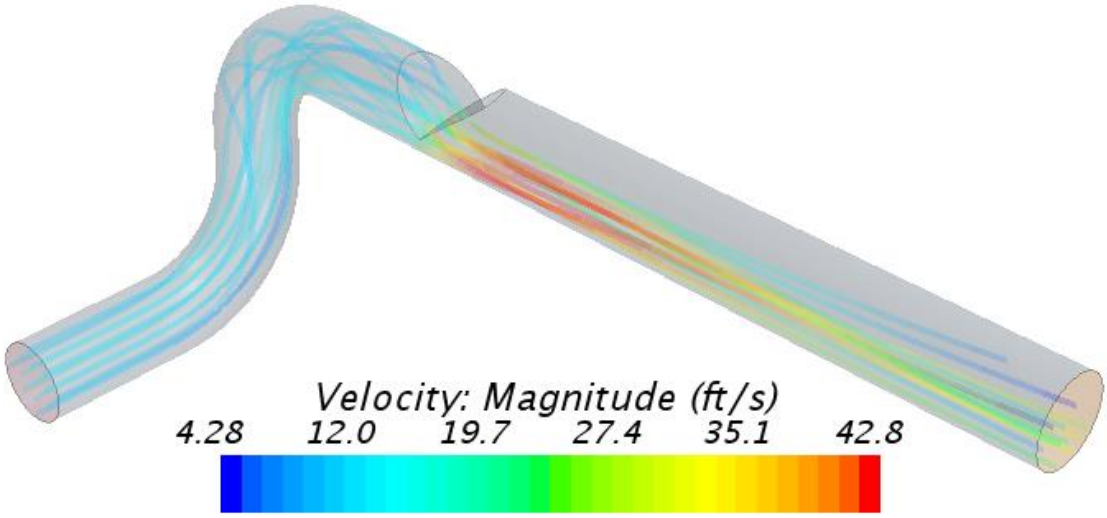

Figure 45: Streamlines, 11 *ft/s*, Close Coupled, Elliptic Blending

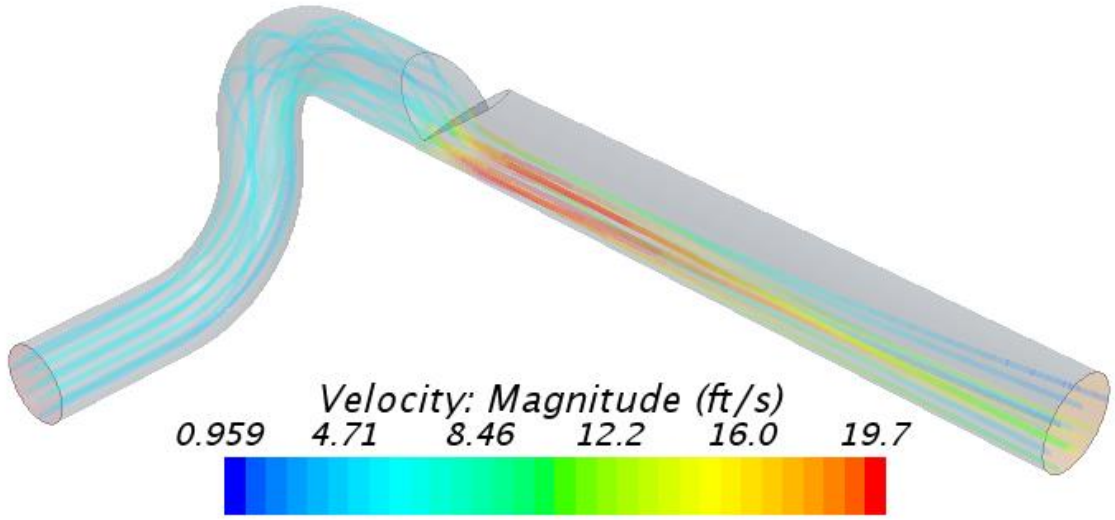

Figure 46: Streamlines, 5 *ft/s*, Close Coupled, Elliptic Blending

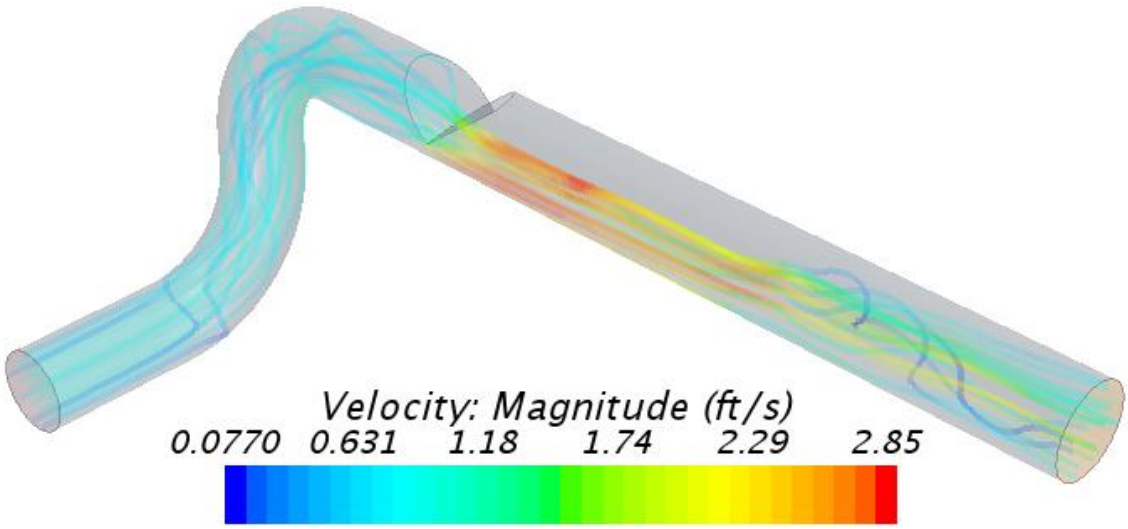

Figure 47: Streamlines, 0.7 *ft/s*, Close Coupled, Elliptic Blending

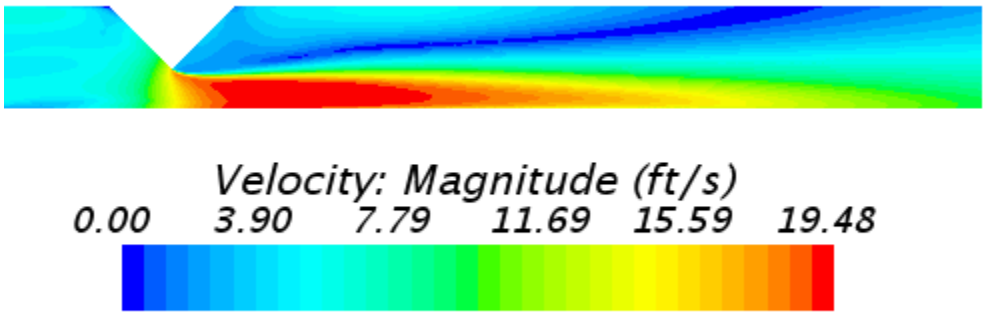

Figure 48: Centerline Velocity Magnitude Contour, 5 *ft/s*, Close Coupled, k-ε

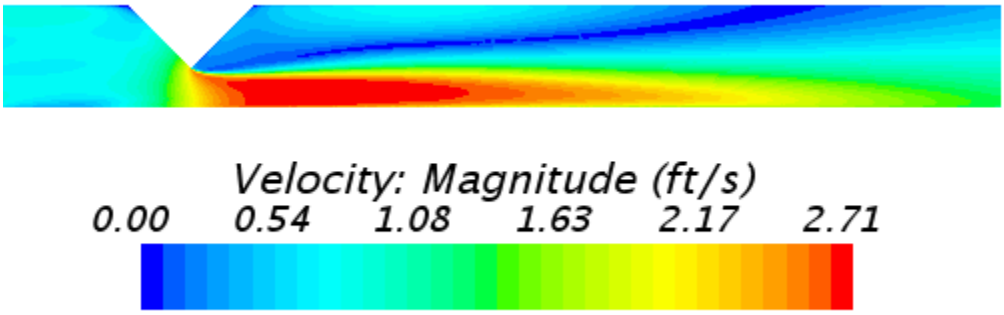

Figure 49: Centerline Velocity Magnitude Contour, 0.7 *ft/s*, Close Coupled, k-ε

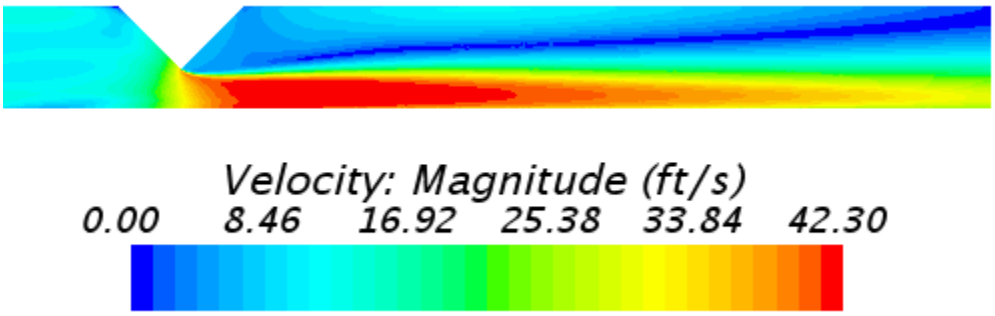

Figure 50: Centerline Velocity Magnitude Contour, 11 *ft/s*, Close Coupled, Elliptic Blending

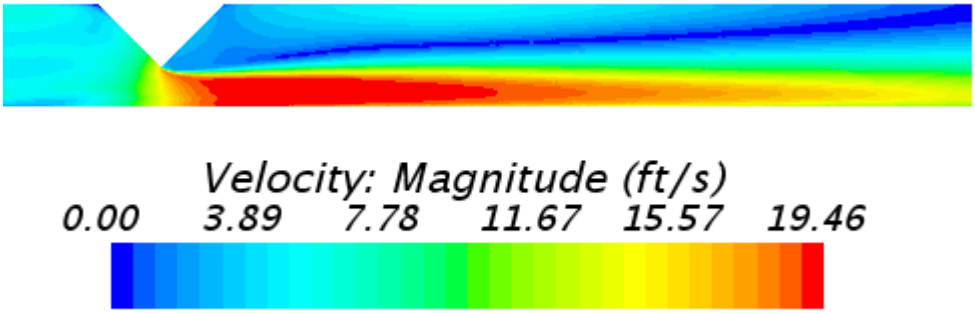

Figure 51: Centerline Velocity Magnitude Contour, 5 *ft/s*, Close Coupled, Elliptic Blending

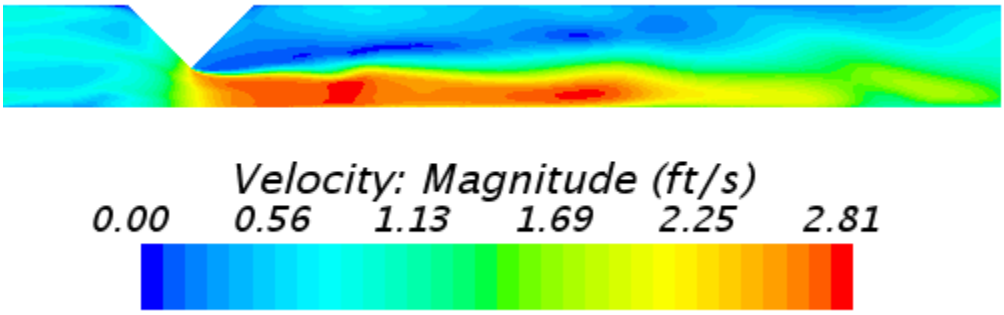

Figure 52: Centerline Velocity Magnitude Contour, 0.7 *ft/s*, Close Coupled, Elliptic Blending

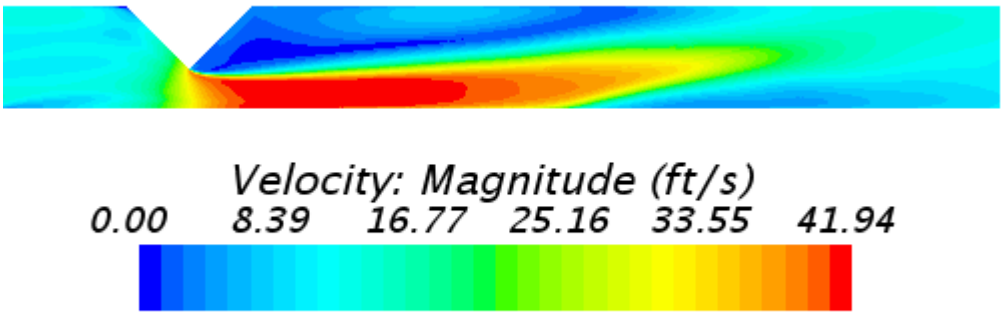

Figure 53: Centerline Velocity Magnitude Contour, 11 *ft/s*, Close Coupled, Reynolds Stress Transport

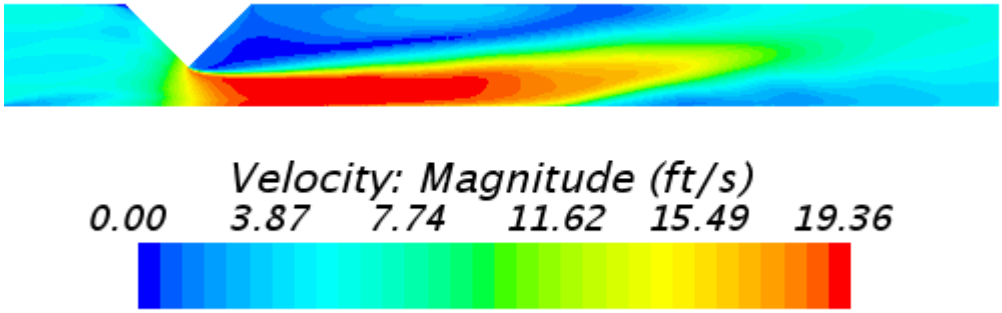

Figure 54: Centerline Velocity Magnitude Contour, 5 *ft/s*, Close Coupled, Reynolds Stress Transport

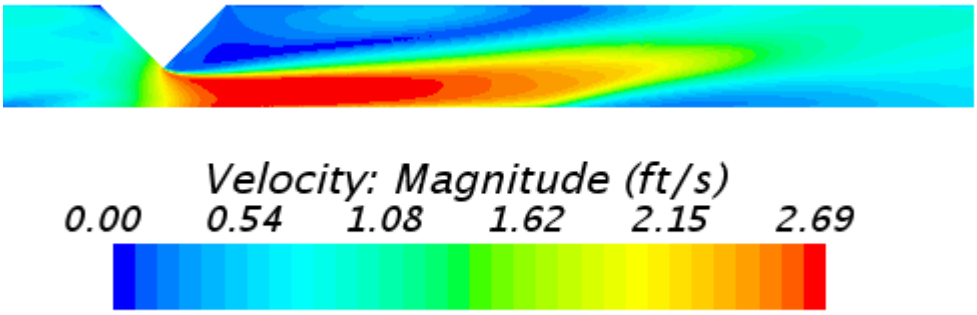

Figure 55: Centerline Velocity Magnitude Contour, 0.7 *ft/s*, Close Coupled, Reynolds Stress Transport

Appendix C: Five Diameter CFD Flow Visualizations

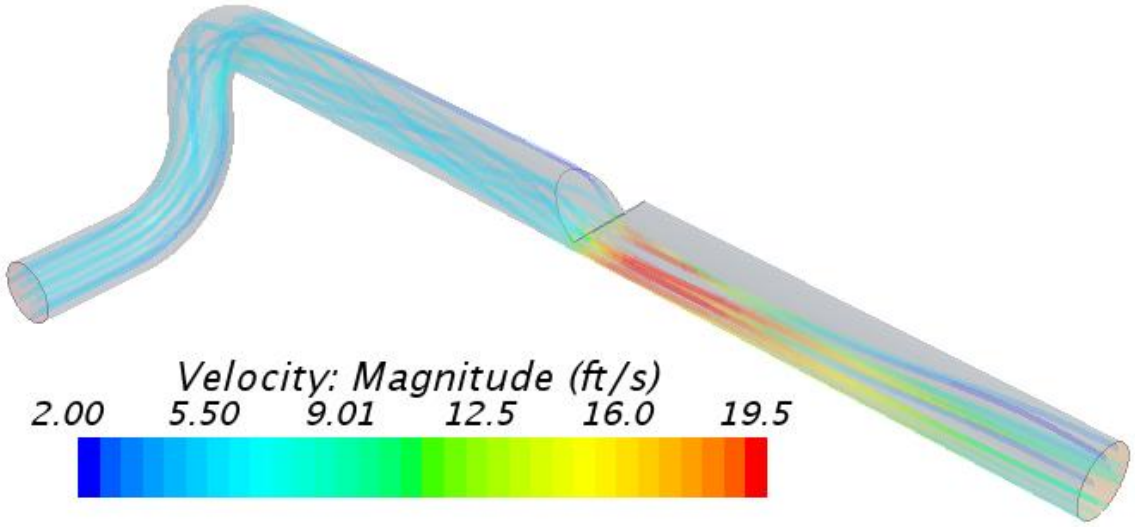

Figure 56: Streamlines, 5 *ft/s*, Five Diameters, k-ε

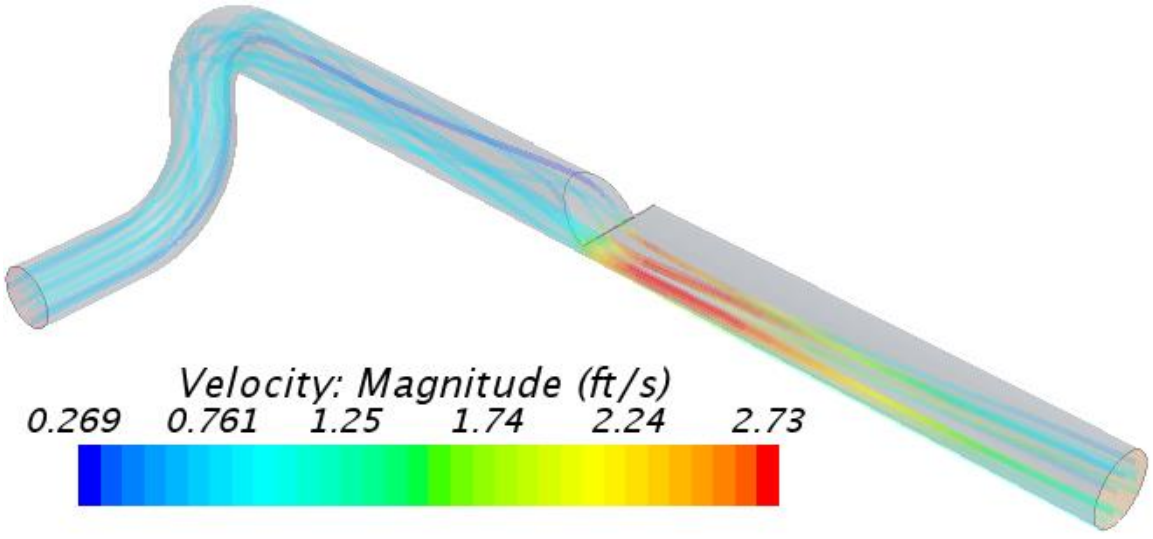

Figure 57: Streamlines, 0.7 *ft/s*, Five Diameters, k-ε

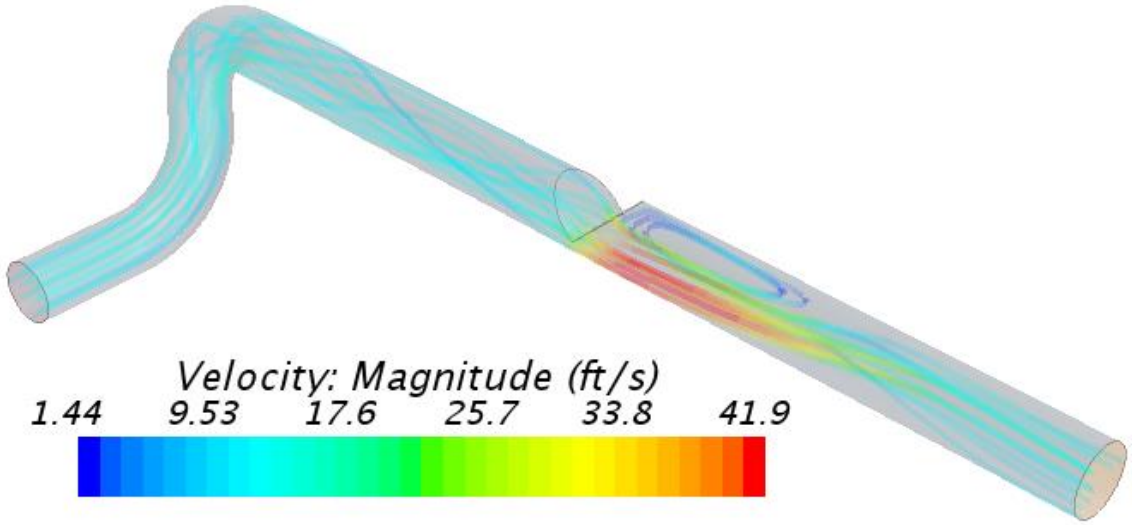

Figure 58: Streamlines, 11 *ft/s*, Five Diameters, Reynolds Stress Transport

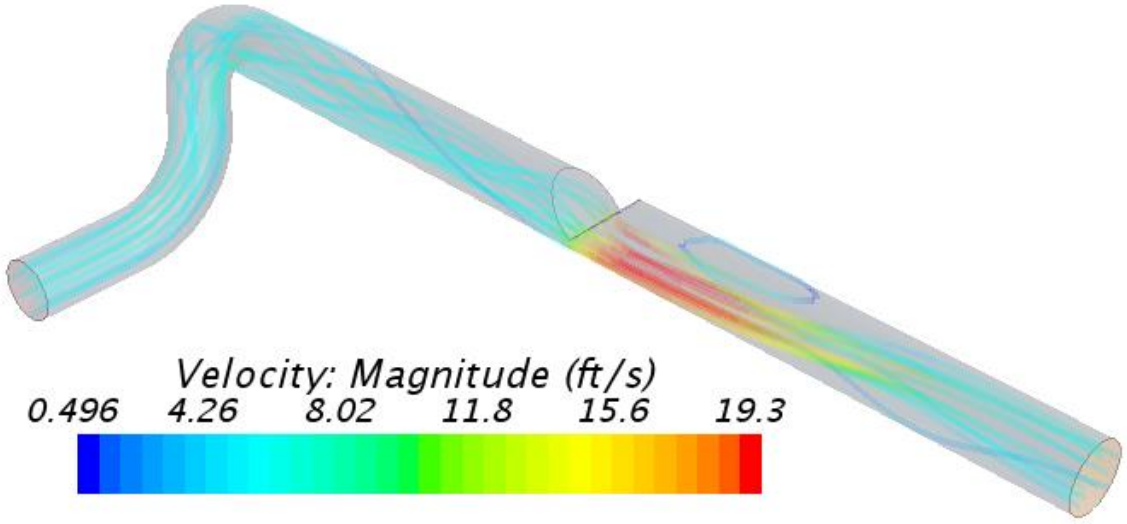

Figure 59: Streamlines, 5 *ft/s*, Five Diameters, Reynold Stress Transport

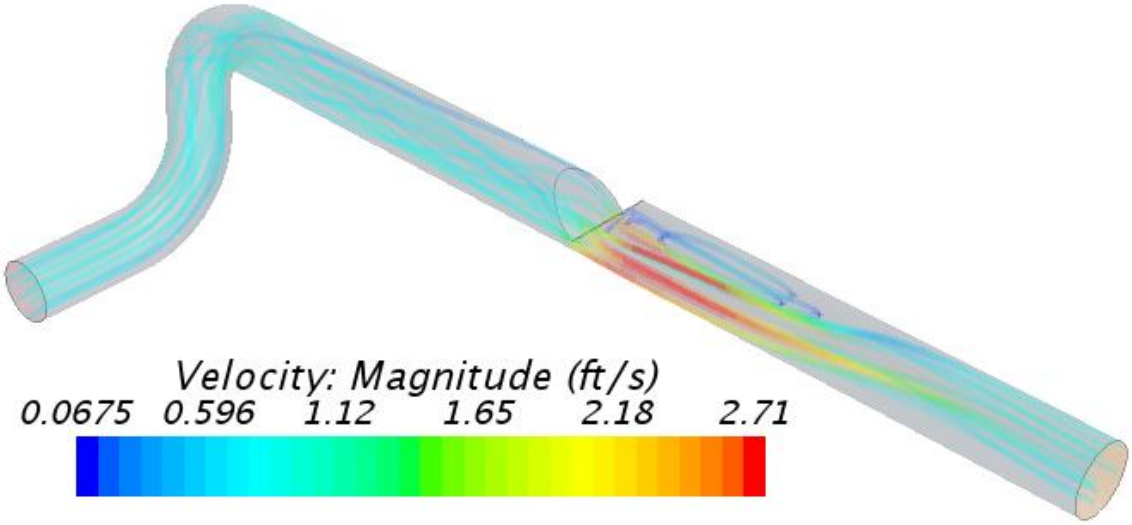

Figure 60: Streamlines, 0.7 *ft/s*, Five Diameters, Reynolds Stress Transport

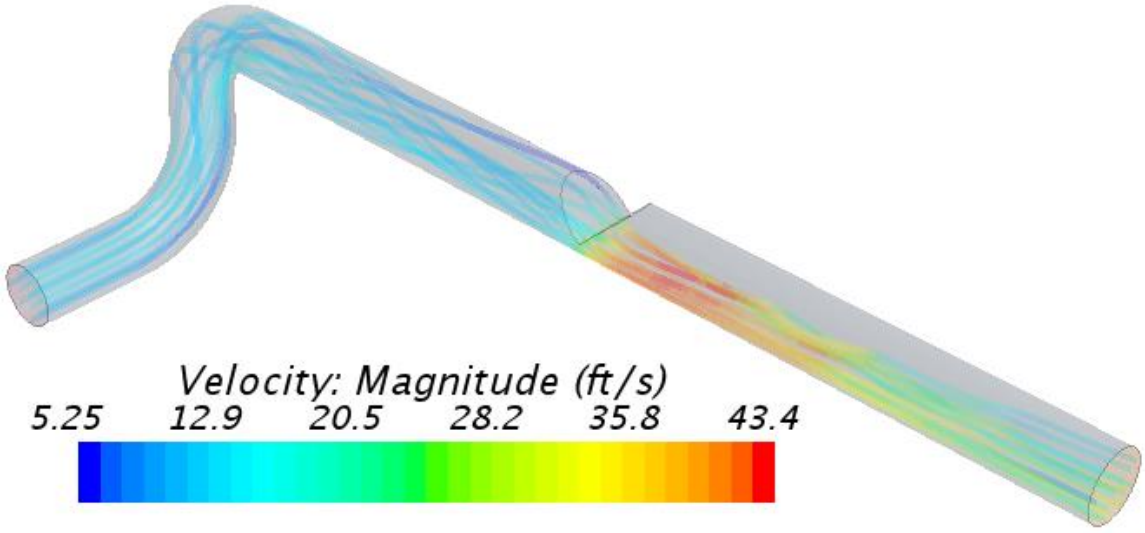

Figure 61: Streamlines, 11*ft/s*, Five Diameters, Elliptic Blending

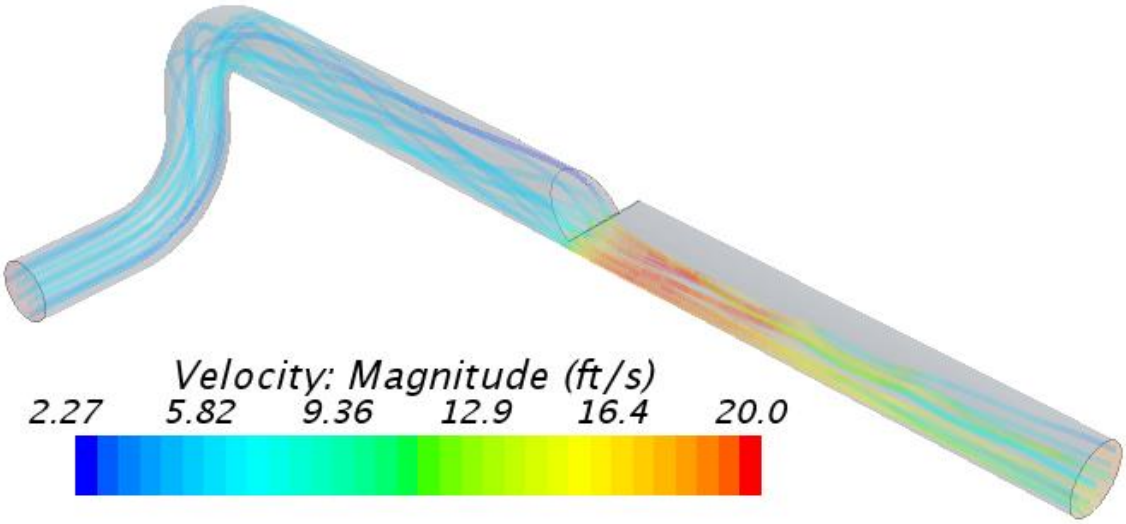

Figure 62: Streamlines, 5 *ft/s*, Five Diameters, Elliptic Blending

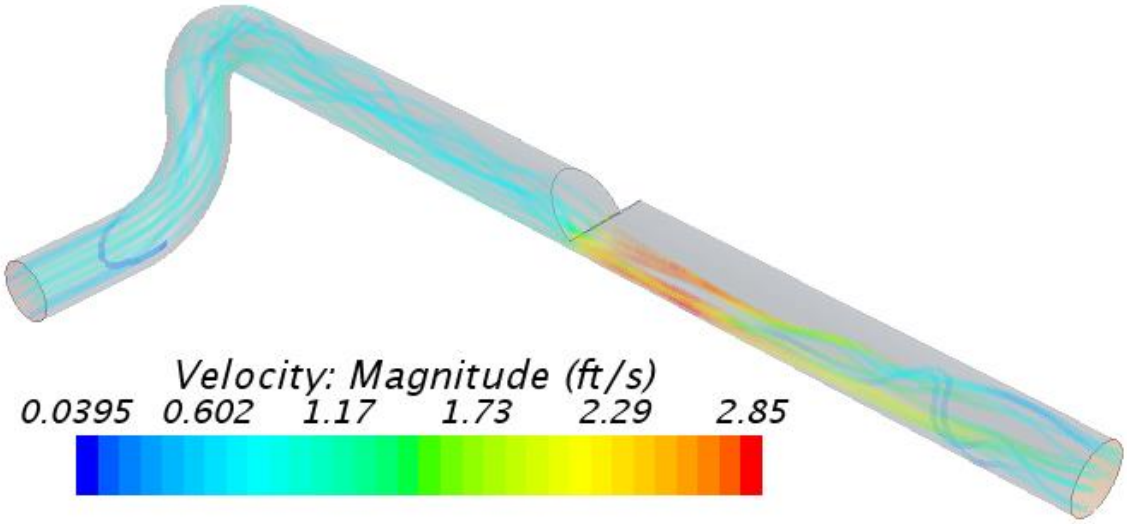

Figure 63: Streamlines, 0.7 *ft/s*, Five Diameters, Elliptic Blending

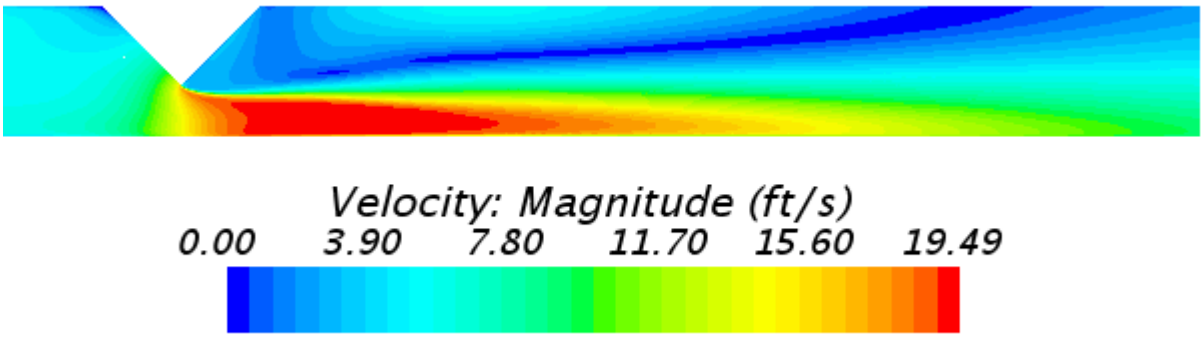

Figure 64: Centerline Velocity Magnitude Contour, 5 *ft/s*, Five Diameters, k-ε

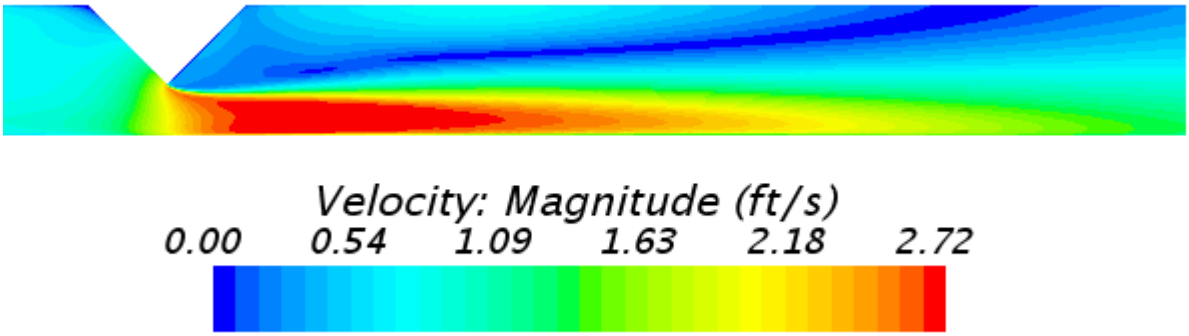

Figure 65: Centerline Velocity Magnitude Contour, 0.7 *ft/s*, Five Diameters, k-ε

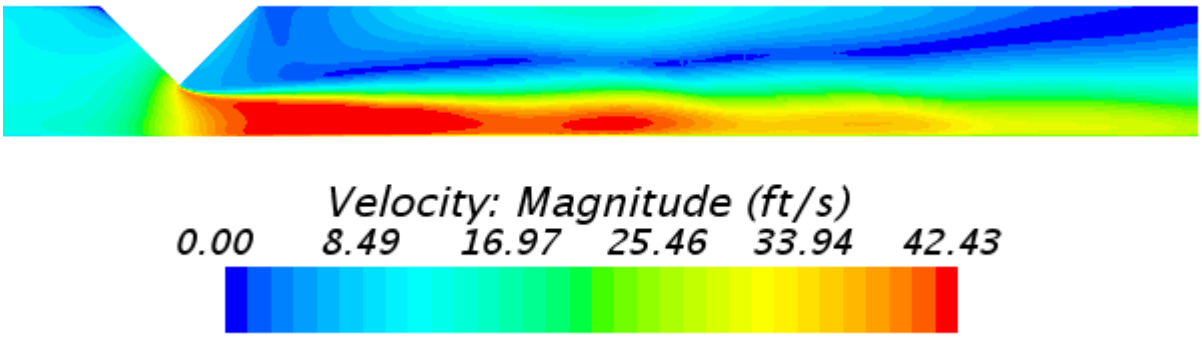

Figure 66: Centerline Velocity Magnitude Contour, 11 *ft/s*, Five Diameters, Elliptic Blending

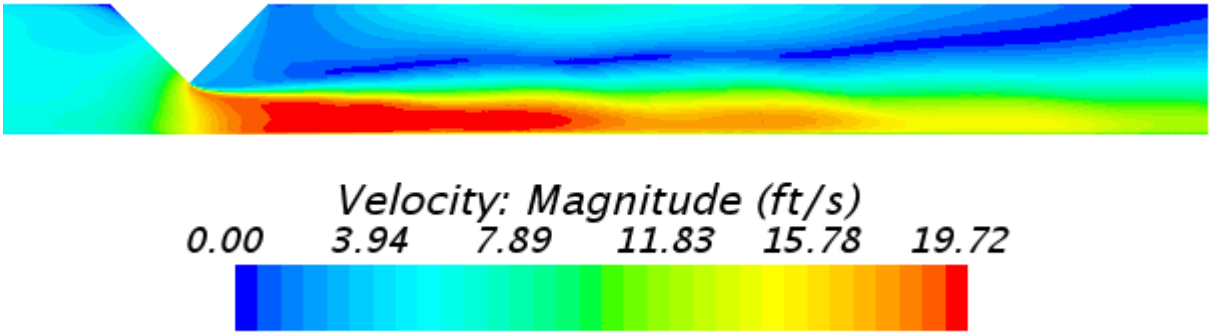

Figure 67: Centerline Velocity Magnitude Contour, 5 *ft/s*, Five Diameters, Elliptic Blending

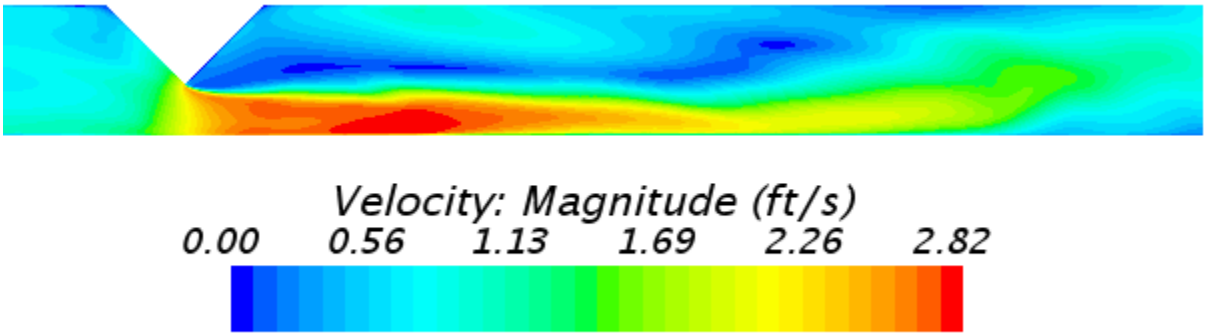

Figure 68: Centerline Velocity Magnitude Contour, 0.7 *ft/s*, Five Diameters, Elliptic Blending

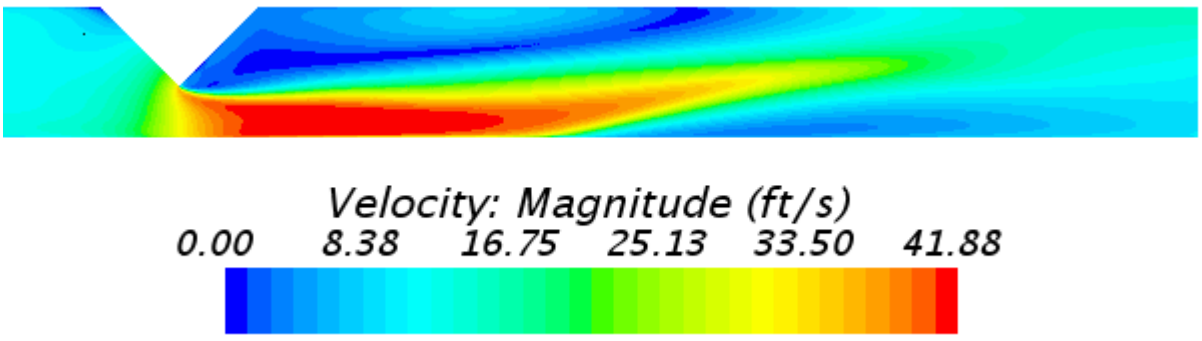

Figure 69: Centerline Velocity Magnitude Contour, 11 *ft/s*, Five Diameters, Reynolds Stress Transport

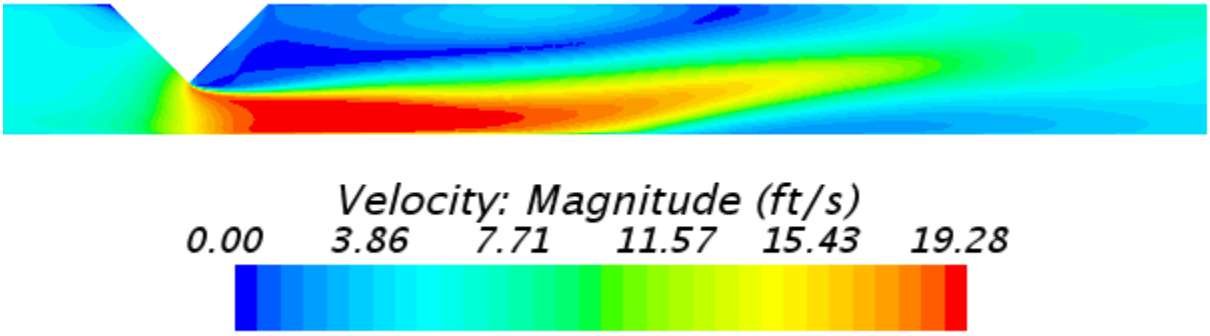

Figure 70: Centerline Velocity Magnitude Contour, 5 *ft/s*, Five Diameters, Reynolds Stress Transport

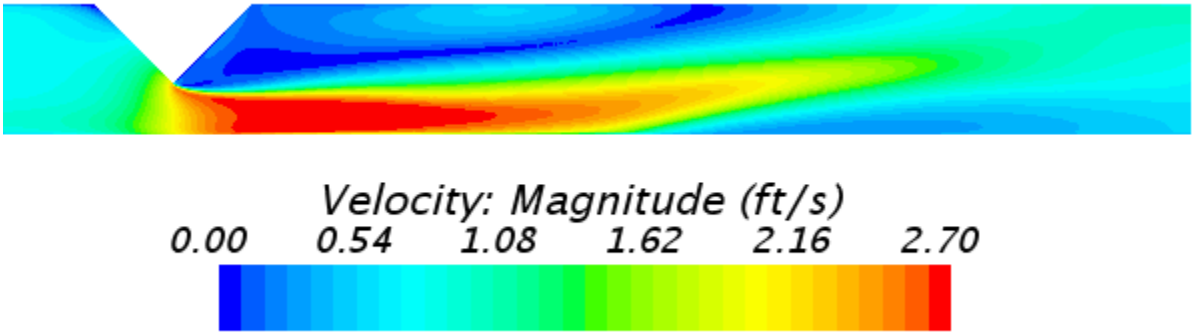

Figure 71: Centerline Velocity Magnitude Contour, 0.7 *ft/s*, Five Diameters, Reynolds Stress Transport

Appendix D: Grid Convergence Index Calculations

```
function [GCIout ] = GCIcalc( N1,N2,N3,Q1,Q2,Q3 )
%GCIcalc This function Calculates the numerical uncertainty
% using the Grid Convergence Index

% ratio of mesh refinement
r21 = (N1/N2)^(1/3);
r32 = (N2/N3)^(1/3);

% variable critical to conclusions
eps21 = Q2-Q1;
eps32 = Q3-Q2;

s = sign(eps32/eps21);

q=0;

% apparent order
p = abs( log(abs(eps32/eps21)) + q )/log(r21);

% fixed point iteration
for i=1:50000
    pold = p;
    q = log( (r21^p - s)/(r32^p-s) );
    p = abs( log(abs(eps32/eps21)) + q )/log(r21);
    if ( abs(p-pold) < 1E-10 )
        break
    end
end

%extrapolated values
Q21_ext = (r21^p*Q1 - Q2)/(r21^p-1);
Q32_ext = (r32^p*Q2 - Q3)/(r32^p-1);

% uncertainty
e21approx = abs((Q1-Q2)/Q1);

e21ext = abs((Q21_ext - Q1)/Q21_ext);

GCI = (1.25*e21approx)/(r21^p-1);

GCIratio(1)=(r21);
GCIratio(2)=(r32);
%output
GCIout(1,:)=[r32,r21,Q3,Q2,Q1,Q21_ext,p,e21approx,e21ext,GCI];

end
```